POLITECNICO
MILANO 1863

SCUOLA DI INGEGNERIA INDUSTRIALE
E DELL'INFORMAZIONE

TeraHertz generation via optical rectification in a GaP crystal for spectroscopy applications

Tesi di Laurea Magistrale in
Electronics Engineering - Ingegneria Elettronica

Author: **Gaia Liso**

Student ID: 970703
Advisor: Prof. Alessio Gambetta
Co-advisors: Prof. Nicola Coluccelli
Academic Year: 2022-23

Abstract

For this master thesis we designed and implemented a system able to generate THz radiation starting from a Yb doped fiber laser emitting ultra-fast pulses. Optical rectification through a GaP crystal was the method chosen to obtain THz radiation whereas electro-optical sampling using another GaP crystal was used for detection. The generating radiation was broadened in frequency using non-linear effects stemming from a silica PCF and dispersion arising from different elements of the setup was compensated using a pair of chirped mirrors. In particular in the thesis we discuss the theoretical basis behind the non-linear processes used, the issues that might affect each process and impair the final result; also possible applications for the system, with a focus on spectroscopy. Finally we present the actual realisation of the setup with the steps taken to optimise the system and ensure good generation and detection. In the end we were able to observe a radiation centered at $3THz$.

Keywords: optical rectification, EO sampling, THz

Abstract in lingua italiana

Per questa tesi magistrale abbiamo realizzato un sistema ottico in grado di generare radiazione THz partendo da un laser a fibra ottica drogata con Yb capace di emettere pulsazioni ultra-veloci. Il metodo scelto per generare radiazione THz è la rettificazione ottica attraverso un cristallo di GaP, invece per la rivelazione della stessa abbiamo usato l'electro-optical sampling utilizzando un altro cristallo di GaP. La radiazione generatrice è stata allargata in frequenza grazie agli effetti non-lineari introdotti da una PCF in silicio, invece la dispersione dreivante dagli elementi del setup è stata compensata utilizzando una coppia di specchi "chirped". In particolare nella tesi discutiamo le basi teoriche dietro i processi non-lineari utilizzati, le problematiche che riguardano ogni processo e il modo in cui impattano il risultato finale; abbiamo anche discusso potenziali applicazioni, focalizzandoci sulla spettroscopia. Infine, presentiamo la realizzazione effettiva del setup e tutti i passaggi seguiti per ottimizzarlo e garantire un buon risultato finale. Il risultato osservato è stato una radiazione centrata in $3THz$.

Parole chiave: rettificazione ottica, EO sampling, THz

Contents

Abstract **i**

Abstract in lingua italiana **iii**

Contents **v**

Introduction **1**

1 THz radiadion: generation, detection and applications **3**

1.1 Optical rectification 3

1.1.1 Phase matching 7

1.1.2 Difference frequency generation (DFG) and intra-pulse DFG (iDFG) 7

1.1.3 Effect of the crystal and of focusing on bandwidth and beam dimension of THz radiation 8

1.1.4 Influence of crystal cut on intensity of generated radiation 12

1.1.5 Crystals for THz generation 14

1.2 Electro-Optical detection of THz radiation 18

1.2.1 Measuring the phase modulation 20

1.2.2 Crystal's geometry influence on THz detection 23

1.2.3 Issues affecting EO sampling 25

1.3 Spectroscopy 26

1.3.1 Influence of noise on THz time domain spectroscopy 28

2 Generation of ultra-short pulses **35**

2.1 Femto-second laser sources and mode locking 35

2.1.1 Fiber lasers 38

2.1.2 Laser RIN 39

2.2 Generation of supercontinuum radiation 40

2.2.1 Silica PCF for supercontimuum generation 42

2.3 Dispersion and compensation 43

3 Experimental results **47**

3.1 Yb fiber laser and photonic crystal fiber 47

3.2 Auto-correlation for pulse duration 50

3.3 Experimental setup used for generation of THz radiation 51

3.4 Experimental setup for detection via EO sampling 55

3.5 Relative intensity noise of the system 58

3.6 Measures and results 60

4 Conclusions and future developments **67**

Bibliography **69**

A Appendix A: methods and instruments **73**

A.1 Golay cell 73

A.2 Lock-in amplifier 74

A.3 Auto-correlator 74

B Appendix B **77**

B.1 Matlab script for measures 77

List of Figures **83**

List of Symbols **87**

Acknowledgements **89**

Introduction

THz radiation is defined as ranging from a frequency of 0.3 THz to 10 THz (wavelength between 1 mm and 30μm), thus occupying the area of the electromagnetic spectrum between infrared and microwave radiation.

Initially, it was used in the astronomy community to study the background of cosmic far-infrared radiation and in the laser-fusion community for the diagnostic of plasmas. In the past years, THz time domain spectroscopy has significantly advanced, helped by the generation of more intense THz fields and detectors with higher sensitivity [26]. It presents applications in medical imaging and diagnostics as its energy spectrum covers that of the collective motion of biological molecules, with the significant advantage that, contrarily to X-rays, it does not ionise molecules [7]; it proves to be particularly useful in the pharmaceutical industry, being used to investigate, in a non destructive way, tablet integrity and performance, and also the presence of impurities in drugs. Another notable way THz radiation can be employed is for security and surveillance: it penetrates fabrics and plastic, making it possible to reveal hidden weapons, without significant risks for people [13].

In this thesis, it will be discussed the generation of THz radiation via optical rectification starting from a high power femto-second Yb doped fibre laser source emitting at a wavelength of 1030 nm, with repetition rate of 25 MHz and average power of 20 W; also its possible use in spectroscopy applications using the detection technique of electro-optical sampling. Particular attention will be put on the characteristics that the generating radiation needs to present: it has to be composed of fast pulses and be broad in frequency domain.

In the first chapter it will be presented the theoretical basis behind optical rectification applied to THz generation, with a section about the crystals generally used for the purpose and the generated field's dependence on their geometry. It will also be presented the theoretical basis behind Electro-Optical (EO) sampling and THz Time Domain Spectroscopy (TDS), together with some notable related issues that may impair results; the second chapter is reserved for the theory behind the generation of super-continuum radia-

tion, with a focus on silica photonic crystal fibers, and compensation of dispersion; in the third chapter we present the system practically implemented, the steps taken to improve it and the final results.

1 | THz radiadion: generation, detection and applications

There are different ways to produce THz radiation: through photoconductive antennas or through second order optical effects, such as difference frequency generation and optical rectification.

Photoconductive antennas are one of the first devices used for this purpose, they consist of two metal electrodes, close but not touching, on a semiconductor substrate. When the antennas act as emitters, they are biased to allow storage of energy in the gap between the two electrodes. When an ultra-fast laser pulse is focused on the gap, a photo-current is generated in the substrate, which emits radiation in the THz range. Instead, when the antennas act as detectors, the ultra-fast laser and THz radiation are focused on the antenna, on different sides, prompting a easily detectable current in the substrate, which is proportional to THz intensity.

Considering non-linear optical effect, it is worth mentioning THz generation via difference frequency generation. For it we need two different monochromatic beams impinging on a non-linear crystal: by choosing their wavelengths it is possible to obtain THz radiation thanks to three wave mixing [11].

The method we used for THz generation is optical rectification through a GaP crystal. In this chapter we present a description of the phenomenon, also focusing on the effect the crystal has on the process. Then we talk about THz detection using electro-optical sampling, again considering how crystal geometry affects measures, and we conclude with a possible application: spectroscopy.

1.1. Optical rectification

Optical rectification is a non linear effect that consists in the generation of a low-frequency polarisation when a powerful enough laser beam passes through a non centro-symmetric crystal.

We want to compute the electric field E_{THz} associated to THz radiation, in order to highlight all the factors influencing it. We can start by saying that when an electric field $\mathbf{E}$ is applied to a non linear dielectric, it becomes polarised, and we can define a linear polarisation density $\boldsymbol{P}_L$, a non linear polarisation density $\boldsymbol{P}_{NL}$ and an electric displacement field $\mathbf{D}$, all related in the following way:

$$\begin{cases} \boldsymbol{P}_L = \epsilon_0 \chi(\omega) \boldsymbol{E}(\omega) & (1.1a) \\ \mathbf{D} = \epsilon_0 \mathbf{E} + \mathbf{P}_L + \boldsymbol{P}_{NL} & (1.1b) \end{cases}$$

Now we rewrite the Maxwell's equations, for simplicity we assume a homogeneous and isotropic medium:

$$\begin{cases} \nabla \cdot \boldsymbol{D} = \rho, & (1.2a) \\ \nabla \times \boldsymbol{E} = -\dfrac{\partial \boldsymbol{B}}{\partial t}, & (1.2b) \\ \nabla \cdot \boldsymbol{B} = 0, & (1.2c) \\ \nabla \times \boldsymbol{B} = \mu_0 (\dfrac{\partial \boldsymbol{D}}{\partial t} + \boldsymbol{J}) & (1.2d) \end{cases}$$

with $\boldsymbol{J} = \sigma_s \boldsymbol{E}$ fictional currents.

After some manipulation of 1.2 and substituting $\mathbf{D}$ and $\mathbf{J}$ with their equations we can finally write the non linear wave equation:

$$\nabla^2 \boldsymbol{E} - \mu_0 \sigma_s \frac{\partial \boldsymbol{E}}{\partial t} - \mu_0 \epsilon \frac{\partial^2 \boldsymbol{E}}{\partial t^2} = \mu_0 \frac{\partial^2 \boldsymbol{P}_{NL}}{\partial t^2} \tag{1.3}$$

which describes the wave's behaviour as it propagates through a non linear medium.

In order to describe the effect of our interest, we need to focus on the non linear term $\boldsymbol{P}_{NL}$, which can be written as a Taylor series given by the formula:

$$\mathbf{P}_{NL}(t) = \epsilon_0 \int \int_{\mathbf{R}^2} \chi^{(2)}(t_1, t_2) \mathbf{E}(t - t_1) \mathbf{E}(t - t_2) dt_1 dt_2 \tag{1.4}$$

where only the second order term of the expansion is being considered as it is the only necessary one to model the optical rectification effect. We can then Fourier transform 1.4 to obtain the equation for polarisation in the frequency domain:

$$P_{NL,i}(\omega) = \epsilon_0 \int_{-\infty}^{+\infty} \chi^{(2)}_{ijk}(\omega; \omega', \omega - \omega') E_j(\omega') E_k(\omega - \omega') d\omega' \tag{1.5}$$

To simplify things we assume a field with fixed polarisation, which can be done without loss of generality, and we write the formula for the electric field of a pulsed beam:

$$E(t) = \frac{1}{2}(E_0(t)e^{j\omega_0 t} + c.c.) \tag{1.6}$$

where $E_0(t)$ is the wave's complex amplitude and ω_0 is the frequency of the carrier. We want to rewrite 1.6 in the frequency domain, so we compute its Fourier transform:

$$E(\omega) = \frac{1}{2}(E_0(\omega - \omega_0) + E_0^*(\omega + \omega_0)) \tag{1.7}$$

which represents the spectrum of the electric field. If the duration $\Delta\tau$ of the laser pulses is much bigger than $\frac{2\pi}{\omega_0}$, then its bandwidth $\Delta\omega$ is much smaller than ω_0. As a result, instead of integrating 1.5 between $+\infty$ and $-\infty$, we can only consider the intervals $(-\omega_0 - \frac{\Delta\omega}{2}, -\omega_0 + \frac{\Delta\omega}{2})$ and $(\omega_0 - \frac{\Delta\omega}{2}, \omega_0 + \frac{\Delta\omega}{2})$; it is relevant to note that not only do we obtain THz radiation, we also observe second harmonic generation. Two of the three frequency ranges obtained are centered at $\pm 2\omega_0$, whereas the last one ranges from $-2\Delta\omega$ to $2\Delta\omega$ and is the one responsible for optical rectification. To further simplify our computations, and assuming to have ω_0 distant from any resonance frequency of the material, we can consider $\chi^{(2)}$ to be constant over said intervals, hence we introduce an effective susceptibility:

$$\chi^{OR}(\omega; \omega_0) = \chi^{(2)}(\omega; \omega', \omega - \omega'), \qquad |\omega_0 - \omega'| \ll \omega_0 \tag{1.8}$$

After substituting 1.7 and 1.8 in 1.5 we finally obtain:

$$P_{OR}(\omega) = \frac{1}{2}\epsilon_0 \chi^{OR}(\omega; \omega_0)(E_0 * E_0^*)(\omega) \tag{1.9}$$

Now, remembering the formula for the intensity of the field

$$I = \frac{\epsilon_0 n(\omega_0) c}{2}(E_0 * E_0^*)(\omega) \tag{1.10}$$

we rewrite the polarisation as a function of intensity:

$$P_{OR}(\omega) = \frac{\chi^{OR}(\omega; \omega_0)}{n(\omega_0)c} I(\omega). \tag{1.11}$$

If we model our pump pulse as a plane wave, propagating perpendicular to the optical and nonlinear polarisation, and we also consider the THz field much weaker than the pump field, then the propagation of the pump can be assumed through a linear medium and

can be written as:

$$I(\omega, z) = I_0(\omega) e^{\frac{j\omega n_g z}{c}} e^{-\alpha_0 z}, \tag{1.12}$$

with α_0 absorption coefficient at ω_0 and $n_g(\omega_0)$ optical group index:

$$n_g(\omega_0) = n(\omega_0) + \omega_0 \frac{\partial n}{\partial \omega}|_{\omega_0}. \tag{1.13}$$

We can now finally rewrite the nonlinear wave equation 1.3 as:

$$\frac{\partial^2 E(\omega)}{\partial z^2} + \left(\frac{\omega^2 n^2(\omega)}{c^2} - j\omega\mu_0\sigma(\omega) \right) E = -\omega^2 \mu_0 \frac{\chi^{OR}(\omega;\omega_0)}{n(\omega_0)c} I(\omega) e^{\frac{j\omega n_g z}{c}} e^{-\alpha_0 z}, \tag{1.14}$$

Where it was used used $c^2 = (\mu_0\epsilon_0)^{-1}$ and $n^2(\omega) = \epsilon(\omega)$. To write the solution to 1.14, we consider waves travelling in the same direction of the pump pulse, also we apply the boundary condition $E(\omega, 0) = 0$ and low THz absorption α_T

$$\alpha_T = \frac{\mu_0 c}{n(\omega)} \sigma(\omega), \tag{1.15}$$

finally obtaining:

$$E(\omega, z) = \frac{\mu_0 \chi^{OR}(\omega;\omega_0)\omega I_0(\omega)}{n(\omega_0)[\frac{c}{\omega}(\frac{\alpha_T(\omega)}{2} + \alpha_0) + j(n(\omega) + n_g)]} \times \tag{1.16a}$$

$$\times \frac{e^{\frac{-j\omega n(\omega) z}{c}} e^{\frac{-\alpha_T(\omega) z}{2}} e^{\frac{-j\omega n_g z}{c}} e^{-\alpha_0 z}}{\frac{\alpha_T(\omega)}{2} - \alpha_0 + j\frac{\omega}{c}(n(\omega) - n_g)}. \tag{1.16b}$$

As expected for nonlinear effects, the THz field increases with χ^{OR} and with pump intensity, it also decreases with absorption both at THz and input pump wavelength; further considerations can be made observing that the second half of 1.16 alone depends on z and, having the unit of a length, we define its absolute value as the effective generation length $L_{gen}(\omega, z)$:

$$L_{gen}(\omega, z) = \left(\frac{e^{-\alpha_T(\omega) z} + e^{-2\alpha_0 z} - 2e^{-\frac{\alpha_T(\omega)}{2} z + \alpha_0 z} cos(\frac{\omega}{c}[n(\omega) - n_g]z)}{[\frac{\alpha_T(\omega)}{2} - \alpha_0]^2 + (\frac{\omega}{c})^2 (n(\omega) - n_g)^2} \right)^{\frac{1}{2}}, \tag{1.17}$$

which has a stronger dependence on linear properties (refractive indices, absorption coefficients) than the rest of 1.16 [19].

1.1.1. Phase matching

The term $n(\omega)-n_g$ gives the amplitude of the THz field, $|E(\omega, z)|$, an oscillatory behaviour (see 1.17); we can avoid this unwanted behaviour by imposing $n(\omega) - n_g = 0$, a condition referred to as phase matching. When the conditions for phase matching are met, all waves participating in optical rectification keep in phase, thus leading to maximum energy conversion coefficient. Given that phase matching happens when the three fields, namely the two generating fields and the THz field, conserve energy and momentum, we can write:

$$\begin{cases} \omega_{opt1} - \omega_{opt2} = \omega_{THz} & (1.18a) \\ k_{opt1} - k_{opt2} = k_{THz}. & (1.18b) \end{cases}$$

Since $\omega_{THz} \ll \omega_{opt}$, and also the two frequencies used to generate THz radiation are very close, we can rewrite 1.18 as:

$$\frac{\partial \omega_{opt}}{\partial k_{opt}} = \frac{\omega_{THz}}{k_{THz}}, \tag{1.19}$$

which is equivalent to saying:

$$v_{g,opt} = v_{ph,THz}, \tag{1.20}$$

with $v_g = \frac{c}{n_g}$. Being the optical frequency much higher than the THz one, THz radiation only sees the profile of the optical one, not its oscillations. To achieve maximum energy conversion, the optical pulse should have a constant temporal delay with respect to the THz pulse along the entire interaction length.

Equation 1.20 gives the collinear phase matching condition, a kind of phase matching which occurs when the excitation and THz beams collinearly propagate through the non-linear crystal. The collinear phase matching guarantees a high generation coefficient, due to long interaction length, and also a good beam quality of the THz radiation [26].

1.1.2. Difference frequency generation (DFG) and intra-pulse DFG (iDFG)

The model for difference frequency generation is the same as the one adopted for optical rectification. We consider $\omega_{opt,1}, \omega_{opt,2}$ angular frequencies of the generating beams and ω, angular frequency of the resulting radiation. It is possible to compute the intensity of the generated radiation as:

$$I_{DFG}(\omega) = \frac{2\omega^2 I_1(\omega_{opt,1}) I_2(\omega_{opt,2}) |\chi^{OR}|^2}{\epsilon_0 c^3 n(\omega_{opt,1}) n(\omega_{opt,2}) n(\omega)} L_{gen}^2, \tag{1.21}$$

which is valid assuming no depletion of the pump, low THz absorption and transparent medium at both $\omega_{opt,1}, \omega_{opt,2}$.

The phase mismatch Δk is different from the one found for optical rectification and can be written as:

$$\Delta k = \frac{1}{c}(\omega n_{THz} - \omega_{opt,2} n(\omega_{opt,2}) + \omega_{opt,1} n(\omega_{opt,1})). \tag{1.22}$$

[11]

Optical rectification and difference frequency generation are actually related processes. In the case of optical rectification, the input pulse envelope varies slowly and induces a DC polarisation that also varies slowly and emits THz or mid-infrared radiation. If the input pulses become shorter, however, the input pulse envelope start to vary faster; considering the frequency domain, the pulses become broader and the frequency components start to interact with each other. One way they interact, and the only one suitable for THz or mid infrared generation, is then by difference frequency generation [1]. The kind of DFG where $\omega_{opt,1}, \omega_{opt,2}$ are taken from the same pulse belonging to an ultra-broadband source is called Intra-pulse DFG (iDFG) [21] .

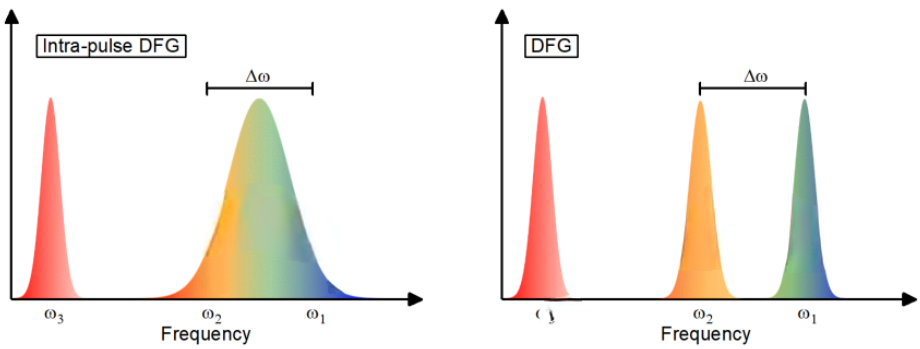

Figure 1.1: Comparison between DFG and iDFG; for iDFG the pump ω_1 and the seed ω_2 come from the same pulse, ω_3, the idler, corresponds to their difference $\Delta\omega$. The frequencies in between do not participate in the process.[1]

1.1.3. Effect of the crystal and of focusing on bandwidth and beam dimension of THz radiation

When the laser beam impinges on the crystal, part of its field is transmitted and part of it is reflected. We can compute the complex Fresnel coefficients for reflection R and

transmission T at the interface between crystal and air:

$$R(\omega) = \frac{2\sqrt{\epsilon_{THz}(\omega)}}{\sqrt{\epsilon_{THz}(\omega)}+1}; \tag{1.23a}$$

$$T(\omega) = \frac{\sqrt{\epsilon_{THz}(\omega)}-1}{\sqrt{\epsilon_{THz}(\omega)}+1}. \tag{1.23b}$$

The inside the crystal behaves as a Fabry-Pèrot etalon, behaviour that translates to the following transmission coefficient:

$$T_{FP} = \frac{T^2(\omega)e^{-j\omega n_{THz}(\omega)\frac{L_{cr}}{c}}}{1-R^2(\omega)e^{-2j\omega n_{THz}(\omega)\frac{L_{cr}}{c}}} \tag{1.24}$$

with L_{cr} length of the crystal. The crystal mostly transmits frequencies for which the relation $2\omega n_{THz}(\omega\frac{L_{cr}}{c}) + \phi(\omega) = 2\pi m$ is valid, being $\phi(\omega)$ the phase of $R^2(\omega)$ and m the order of the mode.

Right outside the crystal, the THz beam start diffracting much faster than a gaussian light beam so, instead of using the Rayleigh method, to compute its aperture during propagation we use Bethe's theory of diffraction by small holes. Being THz radiation dependent on intensity, we can predict that it will be generated by a spot having waist smaller than that of the pump, which will be approximately $w_{THz} = \frac{w_p}{\sqrt{2}}$. What interests us of Bethe's theory is the introduction of the parameter $z_B(\omega)$, similar to the Rayleigh length, which expresses the distance from the waist of a beam at which its cross section is doubled:

$$z_B(\omega) = \frac{k_{THz}^2 w_{THz}^3}{2} = \frac{\omega^2 w_p^3}{4\sqrt{2}c^2}. \tag{1.25}$$

What emerges from this particular length is that lower frequencies diffract faster than what predicted by Rayleigh length z_R (which instead depends on ω^3), however for bigger w_p it becomes negligible with respect to z_R in the bandwidth of interest. We can thus divide the bandwidth in two regions: one in which Bethe's scattering prevails (lower frequencies) and one where Rayleigh scattering better models reality (higher frequencies).

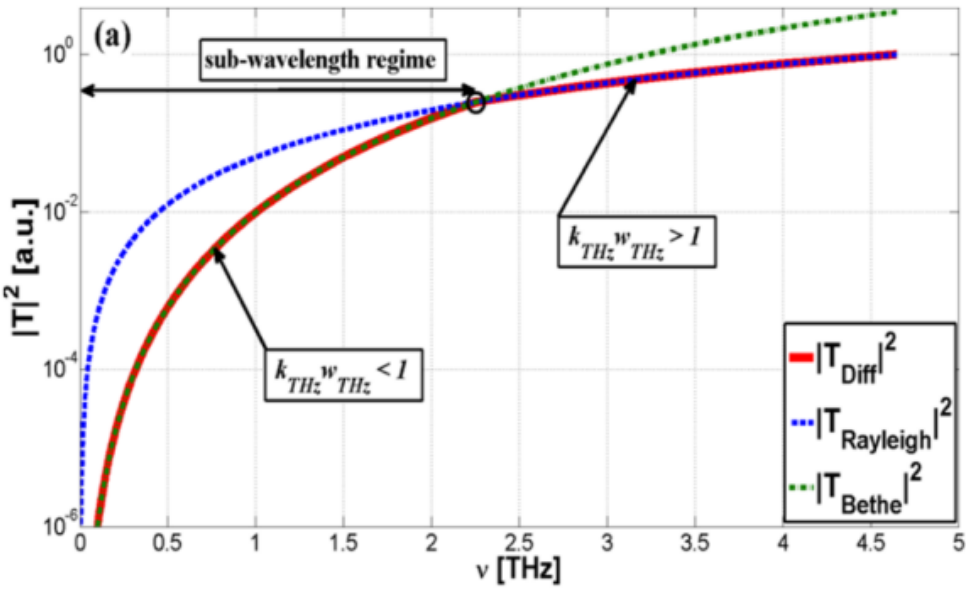

Figure 1.2: Example of diffraction transfer function dependent on frequency, represented with a continuous red line. The frequencies below $2.2THz$, being valid $k_{THz}w_{THz} < 1$ behave as predicted by Bethe's scattering, whereas the frequencies above, when $k_{THz}w_{THz} > 1$, behave as predicted by Rayleigh's scattering.[22]

The result is that the parabolic mirror inserted in the setup to collect THz radiation right after the generating crystal , because of its limited dimension, may not be able to collect the lower frequencies of the THz bandwidth, associated to beams characterised by a big diameter, instead favouring the frequencies affected by Rayleigh scattering.

Another important consideration to make is the effect of the waist beam size w_p on diffraction: as said before, the smaller w_p the more Bethe's scattering is relevant and non negligible.

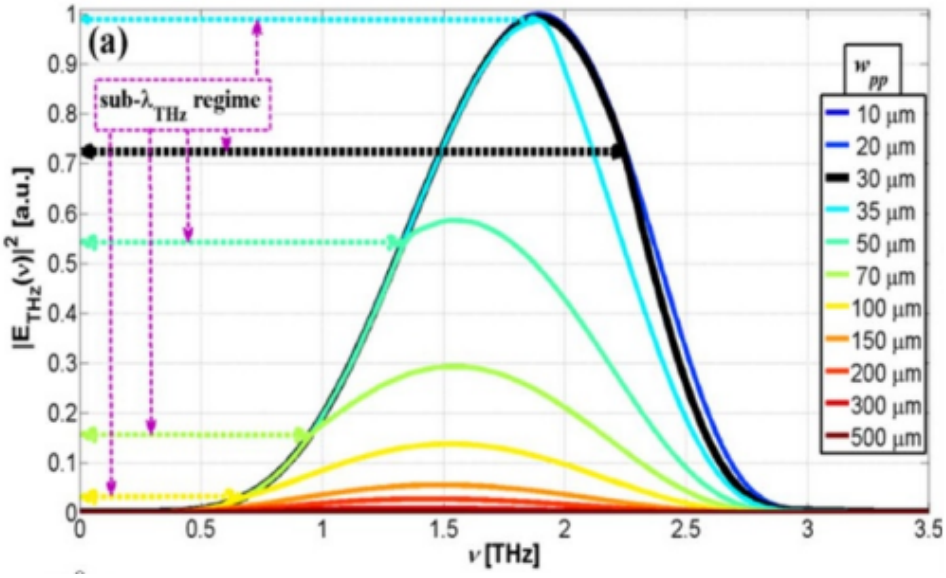

Figure 1.3: Example of how the frequency range affected by Bethe scattering grows with the decrease of the waist beam size. While with smaller beams, a broader frequency range tends to diffract following Bethe's theory, still they produce a stronger THz field compared to larger beams.[22]

However it is worth noting that even if collection of lower frequencies decreases, simulations show that a tightly focused beam impinging on the crystal still generates THz radiation more efficiently than a beam with waist size too big.

Similar problems are encountered when we focus THz radiation on the second crystal, which is necessary for detection: different frequency components are focused to different spot sizes and into different focal planes. We can compute the size of the THz spot arriving to the second mirror which, considering that the lower frequencies of the bandwidth are mostly lost beforehand, is:

$$r_{in}(\omega) = min\left[\frac{D}{2\sqrt{2}}, w_{THz}\sqrt{1+\frac{f^2}{z_{diff}^2}}\right] \tag{1.26}$$

being D and f diameter and focal length of the mirror, z_{diff} confocal parameter (Rayleigh or Bethe, depending on the prevailing diffraction type). Now we can use Gauss' formula to obtain the dimension of the focused THz beam:

$$r_{foc} = \frac{2cf}{\omega r_{in}(\omega)}, \tag{1.27}$$

and then we define the focusing effect as:

$$T_{foc} = \frac{r_{foc}}{r_{in}} = \frac{2cf}{\omega r_{in}^2(\omega)}. \tag{1.28}$$

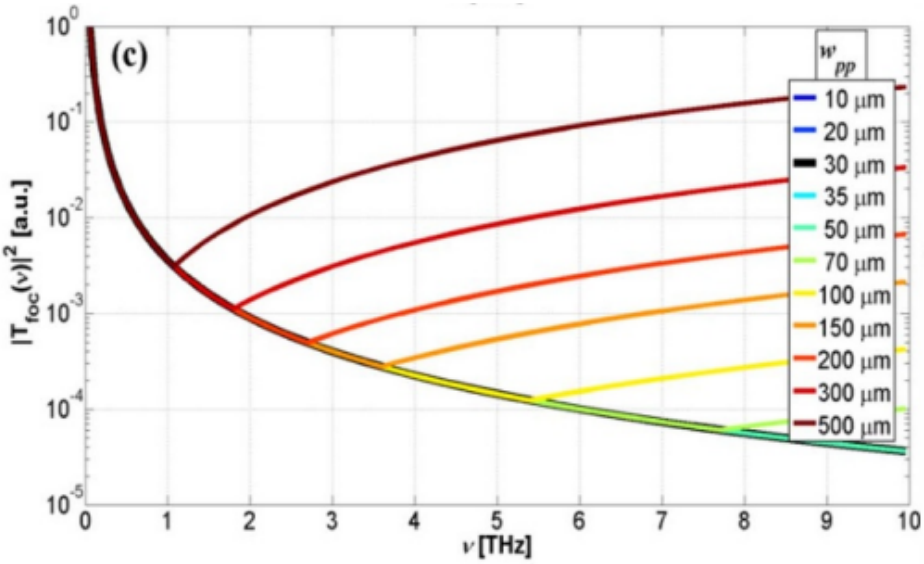

Figure 1.4: Transfer function of the focusing stage, depending on the frequency of the generated radiation and on beam size.[22]

It is interesting to note that lower frequencies are now enhanced, the focusing effect is in fact stronger for wider impinging beams [22] .

1.1.4. Influence of crystal cut on intensity of generated radiation

The polarisation of the generated THz radiation depends on the orientation of the crystal. As a result, also the intensity of the THz radiation is affected by it. The following discussion is valid for zinc-blende crystals, the most common used for THz generation.

For a (110) zinc-blende crystal, the nonlinear susceptibility can be written as:

$$\chi_{ijk} = \chi_{ij} = \begin{bmatrix} 0 & 0 & 0 & \chi_{14} & 0 & 0 \\ 0 & 0 & 0 & 0 & \chi_{14} & 0 \\ 0 & 0 & 0 & 0 & 0 & \chi_{14} \end{bmatrix}, \tag{1.29}$$

the nonlinear polarisation then becomes:

$$\begin{bmatrix} P_x \\ P_y \\ P_z \end{bmatrix} = \begin{bmatrix} 0 & 0 & 0 & \chi_{14} & 0 & 0 \\ 0 & 0 & 0 & 0 & \chi_{14} & 0 \\ 0 & 0 & 0 & 0 & 0 & \chi_{14} \end{bmatrix} \begin{bmatrix} E_x^2 \\ E_y^2 \\ E_z^2 \\ 2E_yE_z \\ 2E_xE_z \\ 2E_xE_y \end{bmatrix}, \tag{1.30}$$

being x, y, z the crystallographic axis $\begin{bmatrix} 1 & 0 & 0 \end{bmatrix}$, $\begin{bmatrix} 0 & 1 & 0 \end{bmatrix}$, $\begin{bmatrix} 0 & 0 & 1 \end{bmatrix}$ respectively.

We consider an electric field E linearly polarised and normally incident on the crystal, so that the field is in the (110) plane and can be written as:

$$\mathbf{E} = E\left(sin\left(\frac{\theta}{\sqrt{2}}\right), -sin\left(\frac{\theta}{\sqrt{2}}\right), cos(\theta)\right), \tag{1.31}$$

where θ is the angle between the polarisation of E_{pump} and the z-axis.

We can then rewrite 1.30:

$$\begin{bmatrix} P_x \\ P_y \\ P_z \end{bmatrix} = 2\chi_{14} \begin{bmatrix} E_yE_z \\ E_xE_z \\ E_xE_y \end{bmatrix} = 2\chi_{14} \begin{bmatrix} -\sqrt{2}sin(\theta)cos(\theta) \\ \sqrt{2}sin(\theta)cos(\theta) \\ -sin^2(\theta) \end{bmatrix}. \tag{1.32}$$

Let us create a reference system $x'y'z'$ by rotating xyz around z by 45°, such rotation corresponds to the following transformation:

$$\begin{bmatrix} x' \\ y' \\ z' \end{bmatrix} = \begin{bmatrix} \frac{1}{\sqrt{2}} & \frac{1}{\sqrt{2}} & 0 \\ -\frac{1}{\sqrt{2}} & \frac{1}{\sqrt{2}} & 0 \\ 0 & 0 & 1 \end{bmatrix} \begin{bmatrix} x \\ y \\ z \end{bmatrix}. \tag{1.33}$$

In the new coordinate system $\mathbf{P}$ is expressed by:

$$\begin{bmatrix} P_{x'} \\ P_{y'} \\ P_{z'} \end{bmatrix} = \begin{bmatrix} P_x + P_y \\ P_x - P_y \\ P_z \end{bmatrix} = \chi_{14}E_0^2 \begin{bmatrix} 0 \\ sin(2\theta) \\ -sin^2(\theta) \end{bmatrix}. \tag{1.34}$$

We know that the electric field of the generated THz radiation is proportional to the nonlinear polarisation, which evidently means that it is also dependent on the angle θ:

$$|E_{THz}| \propto |P| = \chi_{14} E_0^2 (sin^2(\theta)(1 + 3cos^2(\theta)))^{\frac{1}{2}}, \tag{1.35}$$

this expression is maximised when $sin^2(\theta) = \frac{2}{3}$ so $\theta \sim 55°$, reaching the value $E_{THz,MAX} \propto \sqrt{\frac{4}{3}}\chi_{14} E_0^2$ [14].

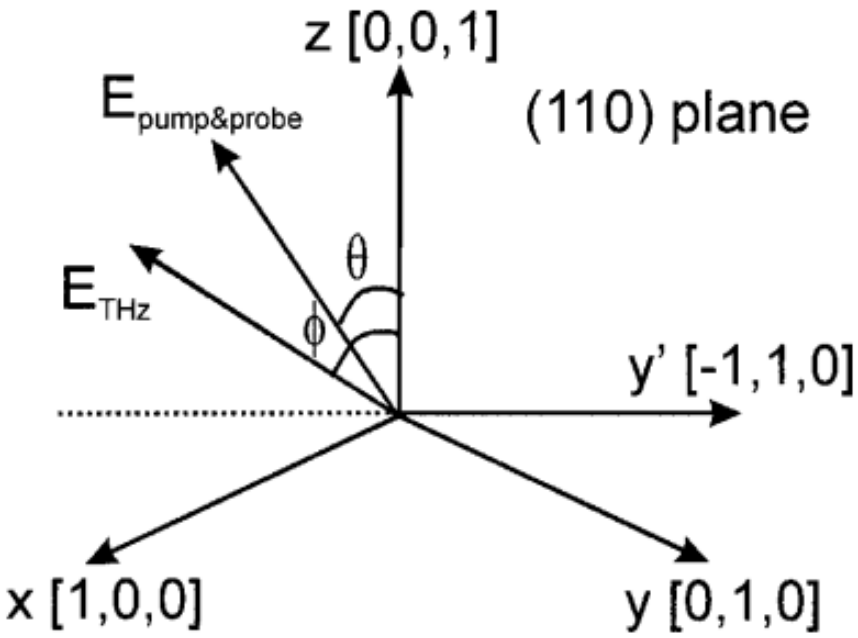

Figure 1.5: Geometry of the (110) zinc-blende crystal. [14]

1.1.5. Crystals for THz generation

When choosing a nonlinear crystal to generate THz radiation, one must consider the magnitude of non linearity of said crystal, which was previously defined as its susceptibility χ^{OR}; in fact, the higher the second order susceptibility, the higher the intensity of the THz radiation (see 1.16). Another important factor to consider before choosing the crystal is the possibility to verify 1.20 during the beams' propagation, so to guarantee phase matching condition.

In order to obtain a wide bandwidth of the THz radiation, achieving phase matching condition may not be enough: if the phonon energy of the crystals used for generation are comparable to the generated frequencies, material absorption will be limiting. We thus need to operate in a zone where the refractive index of the crystal in use is relatively flat.

GaP

One of the most commonly used crystals for THz generation is Gallium Phosphide (GaP), a non birefringent zinc-blende crystal. Some of its most relevant properties are: high second and third order nonlinear susceptibilities $\chi^{(2)}$ and $\chi^{(3)}$; high refractive index; transparency in the range $0.55-11\mu m$ [11, 24]. It is possible to generate THz radiation through it using either collinear or non collinear phase matching, while achieving a high tunability for the central wavelength. GaP is usually pumped with a Nd:YAG laser (1064 µm) but it has also been used in a quasi phase matched regime pumped at 1.55 µm. Experimental results show a bandwidth of the pulsed radiation up to 3.5 THz. If pumped with a 800 nm Ti:Sapphire laser it is possible to have optical rectification phase matched at around 45µm (6.6 THz). At 800 nm GaP shows negligible absorption and a flat refractive index, in the THz range the refractive index is flat before the lowest optical phonon resonance (at room temperature, 10.96 THz).

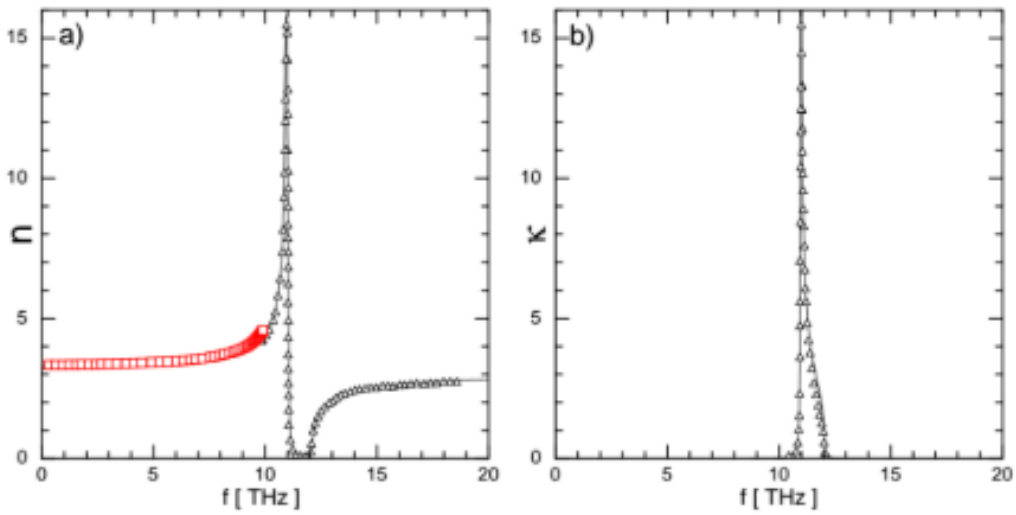

Figure 1.6: Real (left) and imaginary (right) refractive index of GaP. [11]

ZnTe

Zinc Telluride is also a non birefringent zinc-blende crystal. It has been demonstrated that the crystal can generate a pulse having bandwidth of 3 THz. It shows high second order nonlinear susceptibility $\chi^{(2)}$ and favourable phase matching conditions at $800nm$[9, 11]. The biggest problem of ZnTe is phonon absorption, in fact the lowest resonance of its phonons is at 5.4 THz, effectively limiting the obtainable bandwidth.

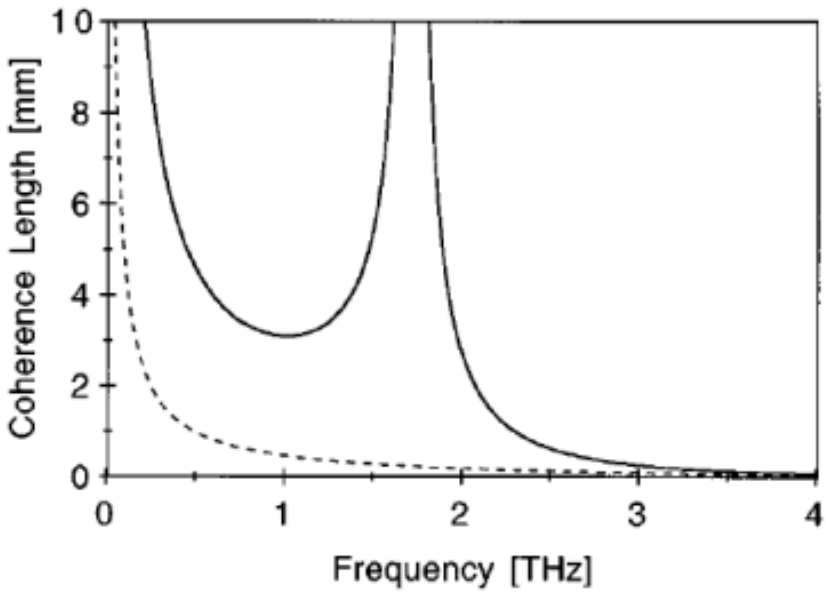

Figure 1.7: Coherence length depending frequency with 800 nm excitation. [11]

CdTe

Cadmium Telluride is another zinc-blende crystal, one of the first one used for THz generation. In general this crystal can generate THz radiation when pumped with radiation having wavelength equal or higher than 700 nm, but for maximum coherence length it is better to use a wavelength of 1050 nm. The generated field is in the range of 1 THz [11]. When pumped by an amplified Yb laser, we see that CdTe is more efficient than GaP for emission at optical fluences lower than 250 $\mu J/cm^2$; However CdTe also presents some limitations when compared with GaP, such as high THz absorption above 1THz and the appearance of two-photon absorption at relatively low optical intensity [18].

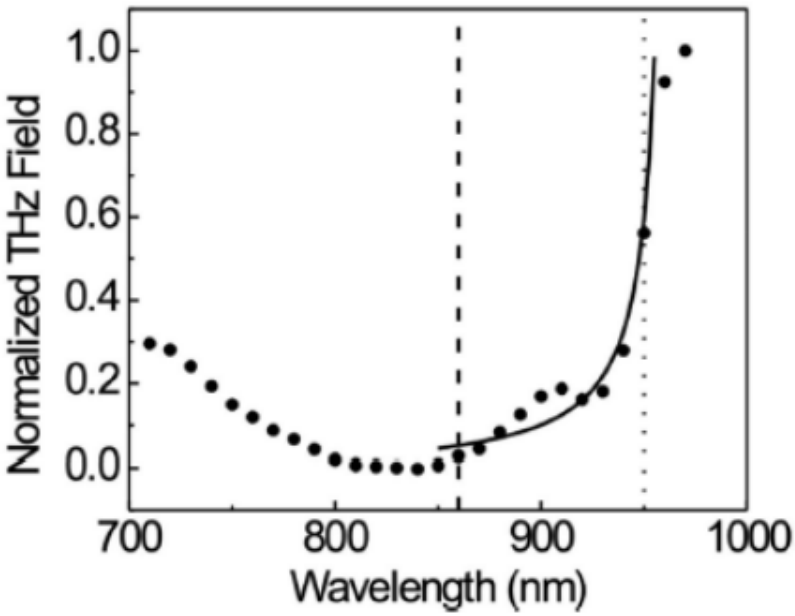

Figure 1.8: THz generation in (110) CdTe with respect to wavelength of pump. [11]

N-dimethylamino-4'-N'-methyl stilbazolium tosylate (DAST)

Organic crystals can have very good nonlinear optical properties, for example larger non-linearity and wider frequency response, sometimes even better than inorganic crystals. Among these organic crystals, N-dimethylamino4'-N'-methyl stilbazolium tosylate (DAST) crystals show significant non-linear optical properties at $\lambda = 1318nm$ and at $\lambda = 720nm$. Pump wavelength usually vary, depending on the cut. The main downside of organic crystals is that many optical phonon resonances are found in The THz range, leading reduced generated THz power in those region of the spectrum [11].

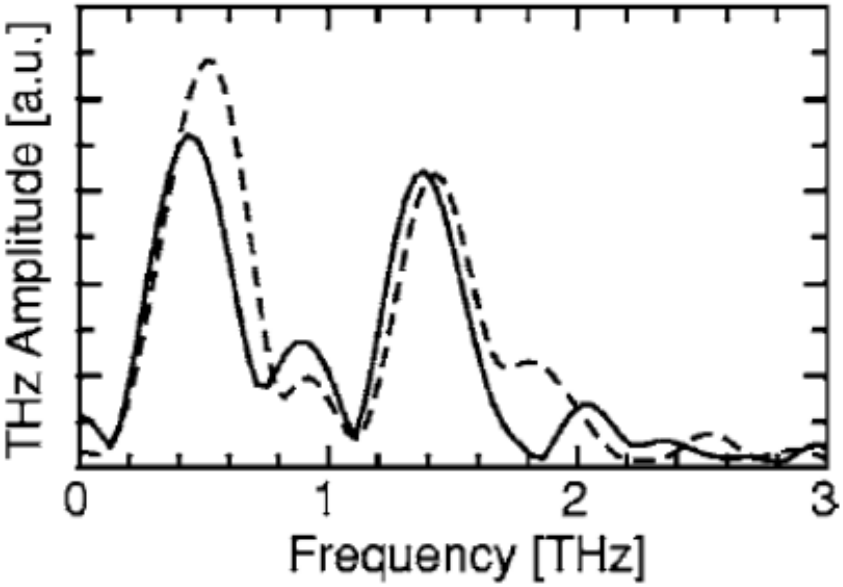

Figure 1.9: Spectra of THz radiation generated in DAST crystal. The solid line corresponds to a pump with $\lambda = 740nm$, the dashed one to a pump with $\lambda = 710nm$.[11]

1.2. Electro-Optical detection of THz radiation

It is possible to detect THz radiation by measuring the phase modulation induced on the reference light pulse by the THz pulse when they propagate through the Electro-Optical crystal at the same time.

During propagation, the two pulses interact generating new frequency components, specifically sum and difference. We can express the considered fields in the following way:

$$E_{THz}(\omega_{THz}, z) = A_{THz}(\omega_{THz}, z)e^{j(k_{THz}z-\omega_{THz}t)}; \tag{1.36a}$$

$$E_{opt}(\omega_{opt}, z) = A_{opt}(\omega_{opt}, z)e^{j(k_{opt}z-(\omega_{opt}-\omega_0)t)}; \tag{1.36b}$$

$$E_{sum}(\omega_{sum}, z) = A_{sum}(\omega_{sum}, z)e^{j(k_{sum}z-(\omega_{sum}-\omega_0)t)}; \tag{1.36c}$$

$$E_{dif}(\omega_{opt}, z) = A_{dif}(\omega_{dif}, z)e^{j(k_{dif}z-(\omega_{dif}-\omega_0)t)}; \tag{1.36d}$$

where ω_0 is the optical carrier frequency, $\omega_{sum} = \omega_{opt} + \omega_{THz}$ and $\omega_{dif} = \omega_{opt} - \omega_{THz}$. After absorption, the wave vectors become complex and can be written as $k = k' + j\beta$.

We can also write the non linear polarisation of the electric field at the sum and difference

frequencies:

$$P^{EO}_{\omega_{sum}} = \chi_{ijk}(\omega_{sum})E_{THz}(\omega_{THz})E_{opt}(\omega_{opt}); \tag{1.37a}$$

$$P^{EO}_{\omega_{dif}} = \chi_{ijk}(\omega_{dif})E^{*}_{THz}(\omega_{THz})E_{opt}(\omega_{opt}); \tag{1.37b}$$

Using the slowly varying amplitude approximation and considering 1.37, it is possible to demonstrate that the expressions for the amplitudes of E_{sum} and E_{dif} are:

$$A_{sum}(l, \omega_{sum} - \omega_0) = j\frac{2\pi\omega^2_{sum}}{c^2 k'_{sum}(\omega_{sum})}\chi_{ijk}(\omega_{sum})\frac{e^{j\Delta k_+ l} - 1}{j\Delta k_+}x \\ xe^{-\beta_{sum}(\omega_{sum})l}A_{THz}(\omega_{THz})A_{opt}(\omega_{opt} - \omega_0); \tag{1.38}$$

$$A_{dif}(l, \omega_{dif} - \omega_0) = j\frac{2\pi\omega^2_{dif}}{c^2 k'_{dif}(\omega_{dif})}\chi_{ijk}(\omega_{dif})\frac{e^{j\Delta k_- l} - 1}{j\Delta k_-}x \\ xe^{-\beta_{dif}(\omega_{dif})l}A^{*}_{THz}(\omega_{THz})A_{opt}(\omega_{opt} - \omega_0); \tag{1.39}$$

where $\Delta k_+ = k_{THz} + k_{opt} - k_{sum}$, $\Delta k_- = -k_{THz} + k_{opt} - k_{dif}$ and l length of the crystal.

For the following calculations, we choose a fixed position $z = 0$ corresponding to the inside face of the crystal and we note that the three electric fields $E_{sum}, E_{dif}, E_{opt}$ propagate at the same frequency ω, being:

$$\omega_{THz} = \Omega, \omega_{opt} = \omega - \Omega; (sum) \tag{1.40a}$$

$$\omega_{THz} = \Omega, \omega_{opt} = \omega + \Omega; (dif) \tag{1.40b}$$

The two fields E_{sum}, E_{dif} are then computed by integration over the bandwidth of the THz radiation:

$$E_{sum}(l, \omega) = j\Big(\int_{-\infty}^{+\infty} \frac{2\pi\omega^2}{c^2 k'_{sum}(\omega)}\chi_{ijk}(\omega; \Omega, \omega - \Omega)\frac{e^{j\Delta k_+ l} - 1}{j\Delta k_+} \\ A_{THz}(\Omega)A_{opt}(\omega - \Omega - \omega_0)e^{-j\Omega\tau}d\Omega\Big)e^{jk_{sum}(\omega)l - j(\omega-\omega_0)t} \tag{1.41}$$

$$E_{dif}(l, \omega) = j\Big(\int_{-\infty}^{+\infty} \frac{2\pi\omega^2}{c^2 k'_{sum}(\omega)}\chi_{ijk}(\omega; \Omega, \omega + \Omega)\frac{e^{j\Delta k_- l} - 1}{j\Delta k_-} \\ A^{*}_{THz}(\Omega)A_{opt}(\omega + \Omega - \omega_0)e^{j\Omega\tau}d\Omega\Big)e^{jk_{dif}(\omega)l - j(\omega-\omega_0)t} \tag{1.42}$$

being τ the delay between the optical and the THz pulses. It is now possible to express the field propagating at ω as the sum of the two fields E_{sum} and E_{dif}. Remembering that $\Delta k_-(-\Omega, \omega) = \Delta k_+(\Omega, \omega)$, $A^{*}_{THz}(-\Omega) = A_{THz}(\Omega)$ and also $\chi_{ijk}(\omega; -\Omega, \omega + \Omega) =$

$\chi^*_{ijk}(\omega;\Omega,\omega+\Omega)$, we are able to simplify the expression and obtain the following:

$$E_{sum}+E_{dif}=j\int_{+\infty}^{-\infty}\frac{2\pi\omega^2}{c^2k'_{sum}(\omega)}e^{jk_{sum}(\omega)l}Re[\chi_{ijk}(\omega;\Omega,\omega-\Omega)]$$
$$\frac{e^{j\Delta k_+(\Omega,\omega)l}-1}{j\Delta k_+(\Omega,\omega)}A_{THz}(\Omega)A_{opt}(\omega-\Omega-\omega_0)e^{-j\Omega\tau-j(\omega-\omega_0)t}d\Omega \quad (1.43)$$

We now introduce the three axes of propagation $\mathbf{e}_x,\mathbf{e}_y,\mathbf{e}_z$: the total field at ω will be given by the vectorial sum of its components propagating in each direction; considering x,y the two direction of polarisation we have:

$$E_x(\omega)=E_{opt,x}(\omega)+E_{sum,x}(\omega)+E_{dif,x}(\omega); \quad (1.44a)$$
$$E_y(\omega)=E_{opt,y}(\omega)+E_{sum,y}(\omega)+E_{dif,y}(\omega); \quad (1.44b)$$

We can see the total field E as the original optical field with its phase modulated by the other propagating fields. Wanting to highlight its component this effect, we write:

$$E_x(\omega)=E_{opt,x}e^{j\phi_x(\omega,\tau)}; \quad (1.45a)$$
$$E_y(\omega)=E_{opt,y}e^{j\phi_y(\omega,\tau)}; \quad (1.45b)$$

considering the phase modulations ϕ_x,ϕ_y smaller than 1, and having expressions:

$$\phi_x(\omega,\tau)=\frac{E_{sum,x}(l,\omega)+E_{dif,x}(l,\omega)}{jE_{opt,x}(\omega)}; \quad (1.46a)$$
$$\phi_y(\omega,\tau)=\frac{E_{sum,y}(l,\omega)+E_{dif,y}(l,\omega)}{jE_{opt,y}(\omega)}; \quad (1.46b)$$

Given that the phase modulations ϕ_x,ϕ_y depend on E_{sum} and E_{dif}, which in turn depend on E_{THz}, by measuring these by ellipsometry it is possible to obtain information on THz radiation.

1.2.1. Measuring the phase modulation

To implement the ellipsometer, it is necessary to use a $\frac{\lambda}{4}$ plane and a Wollaston polariser.

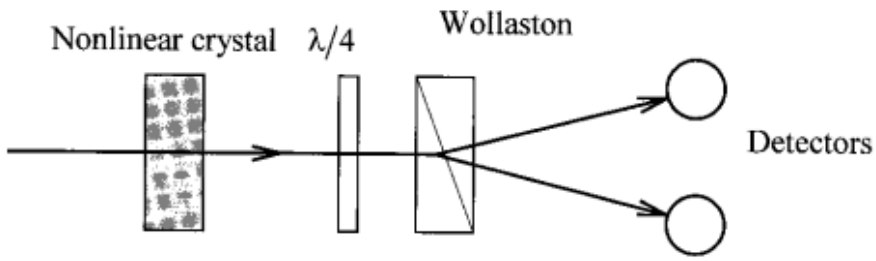

Figure 1.10: General Scheme of an ellipsometer.[4]

We rewrite the field impinging on the $\frac{\lambda}{4}$ plane, referenced to its axis, as:

$$E_x = a_0(\omega)cos(k(\omega)z - \omega t + \phi_x(\omega)); \tag{1.47a}$$
$$E_y = a_0(\omega)cos(k(\omega)z - \omega t + \phi_y(\omega)); \tag{1.47b}$$

The plane adds a $\frac{\pi}{2}$ dephasing on the y-axis, so right after it we have:

$$E_x = a_0(\omega)cos(k(\omega)z - \omega t + \phi_x(\omega)); \tag{1.48a}$$
$$E_y = a_0(\omega)cos(k(\omega)z - \omega t + \phi_y(\omega) + \frac{\pi}{2}); \tag{1.48b}$$

and we can write the axes of the polarisation ellipse as:

$$a(\omega) = a_0(\omega)(1 + \frac{1}{2}\phi(\omega)); \tag{1.49a}$$
$$b(\omega) = a_0(\omega)(1 - \frac{1}{2}\phi(\omega)); \tag{1.49b}$$

with $\phi = \phi_x - \phi_y$ and ϕ small.

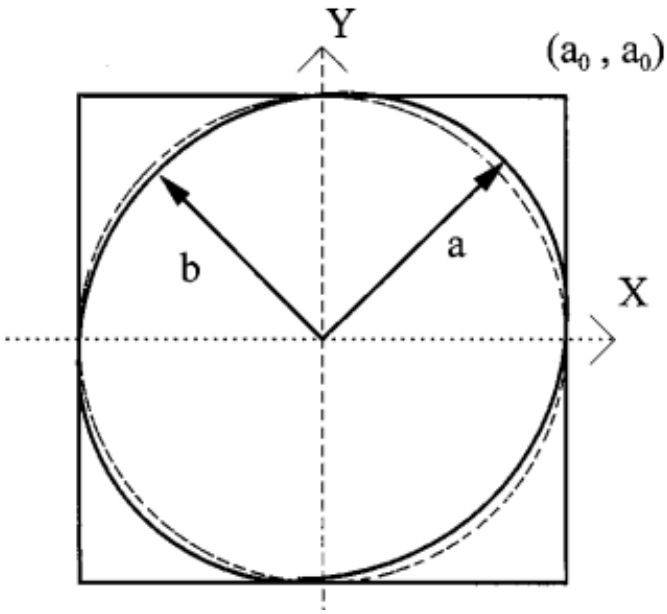

Figure 1.11: Comparison between circular (dashed line) and elliptical polarisation obtained after the $\lambda/4$ plane.[4]

The Wollaston prism is placed right after the plate and is used to divide the two components of the elliptically polarised light, in fact the difference of the components' intensities will be the measured signal. We call the intensities I_a, I_b, then we write them:

$$I_a = \frac{1}{2}\epsilon_0 c \int_{+\infty}^{0} |a(\omega)|^2 d\omega; \tag{1.50a}$$

$$I_b = \frac{1}{2}\epsilon_0 c \int_{+\infty}^{0} |b(\omega)|^2 d\omega; \tag{1.50b}$$

After some manipulation, the resulting signal is:

$$S = I_a - I_b = \epsilon_0 c Re\Big[\int_{+\infty}^{0} |a_0(\omega)|^2 \phi(\omega) d\omega\Big]. \tag{1.51}$$

We now expand the expression of the signal, obtaining:

$$S(\tau) = \frac{1}{2}\epsilon_0 c Re\Big[\int_{+\infty}^{-\infty}\int_{+\infty}^{-\infty} \frac{2\pi\omega^2}{c^2|k'(\omega)|} e^{-2\beta(\omega)l} \chi_{eff}(\omega;\Omega,\omega-\Omega) \frac{e^{j\Delta k_+(\Omega,\omega)l}-1}{j\Delta k_+(\Omega,\omega)} A_{THz}(\Omega) A^*_{opt}(\omega-\omega_0) A_{opt(\omega-\Omega-\omega_0)} e^{-j\Omega\tau} d\Omega d\omega\Big] \tag{1.52}$$

For simplicity we can finally write:

$$S(\tau) = \frac{\pi\epsilon_0}{c}\int_{+\infty}^{-\infty} A_{THz}(\Omega)f(\Omega)e^{-j\Omega\tau}d\Omega \tag{1.53}$$

noting that $f(\Omega)$ is Hermitian so the $Re[]$ can be dropped.

It is relevant to note that $f(\Omega)$ expresses the pulse distortion that is caused by χ_{eff}, absorption of THz radiation by the EO crystal, coherence length and a too temporally broad optical pulse; in fact if $f(\Omega)$ were constant the resulting signal would be a copy of the THz radiation entering the crystal [4].

1.2.2. Crystal's geometry influence on THz detection

Let us consider a (110) zinc-blende EO crystal: when an electric field $\mathbf{E} = (E_x, E_y, E_z)$ is applied to it, the equation of its index ellipsoid becomes:

$$\frac{x^2+y^2+z^2}{n_0^2} + 2\gamma_{41}E_x yz + 2\gamma_{41}E_y zx + 2\gamma_{41}E_z xy = 1, \tag{1.54}$$

with $\gamma_{14} = \frac{-\epsilon_0^2\chi_{14}}{4\pi}$ EO coefficient involved in the Pockels effect. When the THz beam is normally incident on the crystal, the electric field can be written with respect to the crystallographic axes (see 1.1.4) as: $\mathbf{E}_{THz} = E_{THz}(\frac{sin(\phi)}{\sqrt{2}}, -\frac{sin(\phi)}{\sqrt{2}}, cos(\phi))$ so that 1.54 becomes:

$$\frac{x^2+y^2+z^2}{n_0^2} + \frac{2\gamma_{41}E_{THz}sin(\phi)}{\sqrt{2}}yz + \frac{2\gamma_{41}E_{THz}sin(\phi)}{\sqrt{2}}zx + 2\gamma_{41}E_{THz}cos(\phi)xy = 1. \tag{1.55}$$

We can now express 1.55 in the same coordinate system x', y', z' as in section 1.2.2:

$$\frac{x'^2+y'^2+z'^2}{n_0^2} + 2\gamma_{41}E_{THz}sin(\phi)y'z' + \gamma_{41}E_{THz}cos(\phi)(x'^2-y'^2) = 1, \tag{1.56}$$

this way we obtain the equation of the index ellipse in the (110) plane simply by setting $x' = 0$:

$$(\frac{1}{n_0^2} - \gamma_{41}E_{THz}cos(\phi))y'^2 + \frac{z'^2}{n_0^2} + 2\gamma_{41}E_{THz}sin(\phi)y'z' = 1. \tag{1.57}$$

The roots of 1.57 are:

$$s_{1,2} = \frac{1}{n_0^2} + \frac{1}{2}E_{THz}(-cos\phi \pm \sqrt{1+3sin^2(\phi)}) \tag{1.58}$$

and the ellipse in the new plane $y''z''$ is:

$$(\frac{1}{n_0^2} + \frac{1}{2}E_{THz}(-cos\phi + \sqrt{1+3sin^2(\phi)}))y''^2 + \\ + (\frac{1}{n_0^2} + \frac{1}{2}E_{THz}(-cos\phi - \sqrt{1+3sin^2(\phi)}))z''^2 = \frac{y''^2}{n_{y''}^2} + \frac{z''^2}{n_{z''}^2} = 1 \quad (1.59)$$

which gives:

$$n_{y''} \sim n_0 \frac{n_0^3 \gamma_{41} E_{THz}}{4}(cos(\phi) - \sqrt{1+3sin^2(\phi)}) \quad (1.60a)$$

$$n_{z''} \sim n_0 \frac{n_0^3 \gamma_{41} E_{THz}}{4}(cos(\phi) + \sqrt{1+3sin^2(\phi)}) \quad (1.60b)$$

$$\Delta n = (n_{z''} - n_{y''}) = \frac{n_0^3 \gamma_{41} E_{THz}\sqrt{1+3sin^2(\phi)}}{2}). \quad (1.60c)$$

The signal level is proportional to the phase retardation $\Gamma = \frac{2\pi d}{\lambda}\Delta n$, thus:

$$I_{signal} \propto \frac{E_{THz}\sqrt{1+3sin^2(\phi)}}{2} \quad (1.61)$$

To relate the two axes y'', z'' to the coordinate system of $y'z'$ we can compute the eigenvectors of 1.57, obtaining that y'' corresponds to $(1, \frac{2sin(\phi)}{\sqrt{1+3sin^2(\phi)}-cos(\phi)})$ and z'' corresponds to $(1, -\frac{2sin(\phi)}{\sqrt{1+3sin^2(\phi)}+cos(\phi)})$.

The ellipse orientation can then be decided by observing that, being ψ the angle between y'' and y', then $2tan(\phi) = -tan(2\psi)$. When we maximise I_{signal} by setting $\phi = \pm 90°$, it results $\psi = \pm 45°$. Thus for optimal results the polarisation of the probe beam should be parallel to $y'[\pm 1, \mp 0]$ or to $z'[0, 0, \pm 1]$ [14].

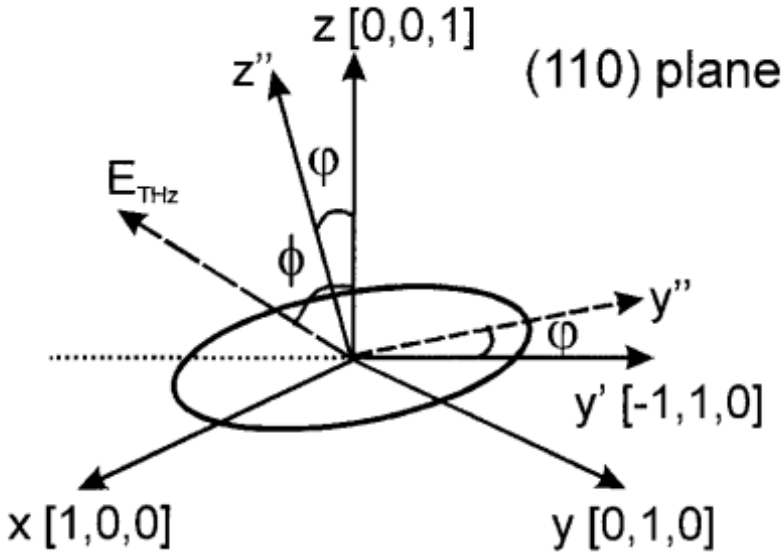

Figure 1.12: Geometry of the (110) crystal for EO sampling.[14]

1.2.3. Issues affecting EO sampling

EO sampling is a simple mechanism offering the advantage of being able to detect with great accuracy amplitude and phase of the pulses under investigation, but still it presents some issues, mostly similar to the ones affecting optical rectification: dispersion and absorption inside the crystal and at the air-crystal interface; Fabry-Pèrot effect inside the crystal; finite pulse duration of the probe; phase mismatch between THz radiation and probe beam; imperfect overlapping between THz radiation and probe beam.

The first two issues are modeled in the same way as for the generation case (see 1.1.3); to account for the finite pulse duration of the probe beam and phase mismatch between it and the THz beam, we can write the following frequency response:

$$F(\omega) = A_{opt}(\omega)\chi^{(2)}(\omega_p; \omega, \omega_p - \omega)\Delta\phi(\omega) \tag{1.62}$$

with $A_{opt}(\omega)$ auto-correlation of the Gaussian probe pulse, $\Delta\phi(\omega)$ phase mismatch factor which can be expressed as:

$$A_{opt}(\omega) = \frac{\sqrt{\pi}}{\tau_p} e^{-\frac{\omega^2 \tau_p^2}{4}} \tag{1.63a}$$

$$\Delta\phi(\omega) = \frac{e^{-j\Delta k(\omega) L_{det}} - 1}{j\Delta k(\omega)} \tag{1.63b}$$

having τ_p duration of the probe pulse, $\Delta k(\omega) = k_p(\omega_p) + k(\omega) - k_p(\omega_p - \omega)$ mismatch

between the wave vectors of the probe field, THz field and frequency-difference field, and L_{det} length of the detection crystal.

The last issue, overlapping of THz field and probe field, stems form the fact that the focusing of THz is frequency dependent: the THz beam is broadband so it can be considered itself as the overlapping of many single-frequency beams with different waist sizes (see 1.1.3). It is thus evident that the frequencies detected with better efficiency will be the ones with spot size more overlapped with the probe's one. We can express this effect as:

$$T_{overlap}(\omega) \propto \int_{-\infty}^{+\infty} |E_p(r)|^2 E_{THz} dr = \sqrt{\frac{\pi w_p^2 r_{foc}^2(\omega)}{w_p^2 + 2r_{foc}^2(\omega)}}. \tag{1.64}$$

[22]

1.3. Spectroscopy

It is possible to use THz radiation for spectroscopy. The goal of a THz spectrometer is to measure the complex and frequency dependent refractive index of the sample in analysis; while its real part might be used for measuring the thickness of the sample, its imaginary part is related to the absorption coefficient so that $\alpha_T = \frac{2\omega k}{c}$, being $n = n_r + jk$ [3, 6].

We are able to retrieve information on n by observing the behaviour of radiation passing through the sample. In general, we obtain the final result by performing the ratio between the field passing through the sample and a reference one.

Let us consider the following system:

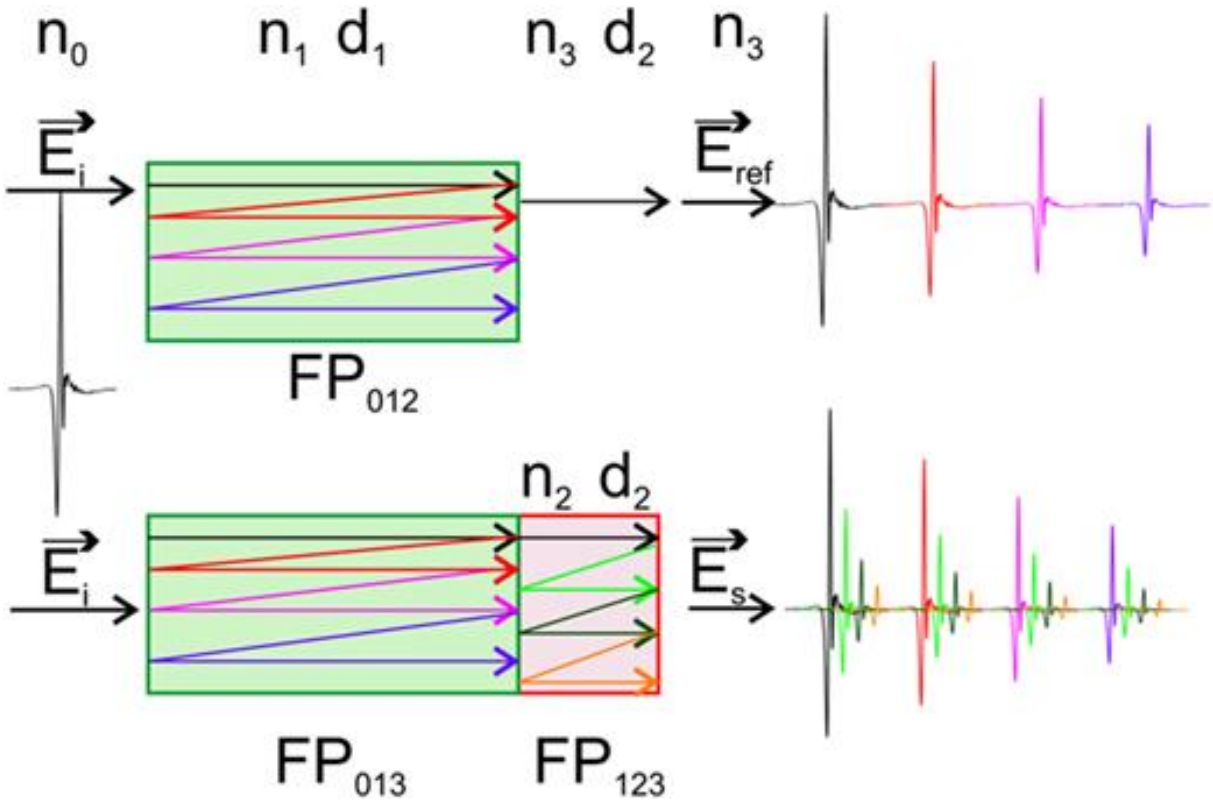

Figure 1.13: Example of a two layer system used for THz spectroscopy. The system can be considered to be in air ($n_0 = n_3 = 1$) for simplicity. n_1, d_1 refer to the substrate while n_2, d_2 refer to the sample under observation.[6]

The reference consists of a single layer with refractive index n_1 and depth d_1, as shown at the top of the image; the layer of interest, characterised by refractive index n_2 and depth d_2 is then added on top of the reference substrate, as shown at the bottom of the image. For simplicity, we can consider that n_0 and n_3 are the same and are the refractive index of air.

We can write the transfer function for the sample:

$$E_s = t_{01} P_1 t_{12} P_2 t_{23} FP_{012} FP123 E_i, \tag{1.65}$$

where E_i is the input electric field, t_{jk} is the complex transmission Fresnel coefficient with expression:

$$t_{jk} = \frac{2n_j}{n_j + n_k}, \tag{1.66}$$

P_j represents the propagation through a layer which can be written as $e^{-ik_0 d_j n_j}$, finally FP_{jkl} is the Fabry-Pérot etalon caused by M partial reflections of the pulse, having

expression:

$$FP_{jkl} = \sum_{m=0}^{M} (r_{jk} r_{kl} P_k^2)^m \tag{1.67}$$

where $r_{jk} = \frac{n_j - n_k}{n_k + n_j}$ is the complex reflection Fresnel coefficient.

Now we write the reference transfer function:

$$E_{ref} = t_{01} P_1 t_{13} P_3 FP_{012} E_i, \tag{1.68}$$

and we compute the ratio between the two which, after simplifying, becomes:

$$\frac{E_s}{E_{ref}} = \frac{t_{12} t_{23}}{t_{13}} \frac{P_2}{P_3} \frac{FP_{012} FP_{123}}{FP_{013}}. \tag{1.69a}$$

It is then possible, being known all thicknesses and other refractive indexes, to compute the refractive index of the substrate n_2 [6].

1.3.1. Influence of noise on THz time domain spectroscopy

There are many noise sources affecting THz-TDS: laser intensity fluctations, optical and electronic noise, delay line jitter but also errors in the measure of the sample's thickness, sample misalignment and so on. All the aforementioned errors and noise sources introduce a certain degree of uncertainty to the measure we obtain at the output of our system [25].

In order to model said uncertainty, we start by recalling equation 1.65 and simplifying the system: we ignore layer 1 and consider a system with a single layer corresponding to the sample put in air. The new equation for the transmitted field E_s is:

$$E_s(\omega) = E_i(\omega) t_{2,0}(\omega) P_2(\omega, d_2) FP_{20} \tag{1.70}$$

where now $FP_{20} = \sum_{p=0}^{+\infty} (r_{2,0}(\omega) P^2(\omega, d_2))^p$.

The signal directly transmitted through the sample corresponds to the one where $p = 0$, the other terms of the summation are temporal echoes. If the recorded signal goes to zero between an echo and another, then we can use anyone of them to compute the material parameters. We can then write the modulus and the argument of the transmission

coefficient $T(p,\omega)$ for each echo:

$$\rho(p,\omega) = |T(p,\omega)| = \frac{4\sqrt{n_r^2+k^2}((n_r-1)^2+k^2)^p}{(n_r+1)^2+k^2)^{p+1}} \times \\ \times e^{-k(2p+1)\frac{\omega d_2}{c}} \tag{1.71}$$

$$\psi(p,\omega) = arg[T(p,\omega)] = -(((2p+1)n_r-1)\frac{\omega d_2}{c} - 2p)\times \\ \times arctg(\frac{2k}{n_r^2+k^2-1}) - arctg(\frac{k}{n_r(n_r+1)+k^2}) \tag{1.72}$$

where $n_0 = 1$.

For most materials $k \ll n$, thus we obtain the refractive index n_r and the energy absorption coefficients $\alpha = \frac{2\omega k}{c}$:

$$n_r = \frac{1-\frac{c}{\omega d_2}\psi(p,\omega)}{2p+1} \tag{1.73a}$$

$$\alpha = \frac{-2}{(2p-1)d_2} ln\left(\frac{(n_r+1)^{2p+2}}{4n_r(n_r-1)^{2p}}\rho(p,\omega)\right), \tag{1.73b}$$

from which we derive the errors Δn_r and $\Delta\alpha$:

$$\Delta n_r = \frac{c}{(2p+1)\omega d_2}\Delta\psi(p,\omega) \tag{1.74a}$$

$$\Delta\alpha = \frac{2}{(2p+1)d_2}\left(\left|\frac{(n_r-1)^2-4pn_r}{n_r(n_r^2-1)}\right|\Delta n_r + \frac{\Delta\rho(p,\omega)}{\rho(p,\omega)}\right) \tag{1.74b}$$

where errors $\Delta\rho, \Delta\psi$ are obtained from the standard deviation of the experimental transmission coefficient $T_{exp}(p,\omega)$. In fact we can write $T_{exp}(p,\omega)$ as the sum of its average value plus a random contribution coming from noise:

$$T_{exp}(p,\omega) = T(p,\omega) + T_N(p,\omega) = \tag{1.75}$$

$$= \rho(p,\omega)e^{j\psi(p,\omega)} + \rho_N(p,\omega)e^{j\psi_N(p,\omega)}; \tag{1.76}$$

considering a noise much lower than the signal we write the new argument and modulus of the transmission coefficient $\rho_{exp}(p,\omega), \psi_{exp}(p,\omega)$:

$$\rho_{exp}(p,\omega) = \rho(p,\omega) + \rho_N(p,\omega)(cos(\psi()p,\omega) - \psi_N(p,\omega)), \tag{1.77a}$$

$$\psi_{exp}(p,\omega) = arctg\left(\frac{\rho(p,\omega)sin(\psi(p,\omega)+\rho_N(p,\omega)sin(\psi_N(p,\omega))}{\rho(p,\omega)cos(\psi(p,\omega)+\rho_N(p,\omega)cos(\psi_N(p,\omega))}\right). \tag{1.77b}$$

Assuming uncorrelated noise on the modulus and on the argument, we get the variances associated to ρ and ψ:

$$s_\rho^2(p,\omega) = \frac{< \rho_N^2(p,\omega) >}{2}, \tag{1.78a}$$

$$s_\psi^2(p,\omega) = \frac{s_\rho(p,\omega)}{\rho(p,\omega)}. \tag{1.78b}$$

which allow us to rewrite 1.74 as:

$$\Delta n_r = \frac{c}{(2p+1)\omega d_2}\frac{s_\rho(p,\omega)}{\rho(p,\omega)} \tag{1.79a}$$

$$\Delta\alpha = 2\Delta n_r\left(\frac{\omega}{c} + \frac{1}{(2p+1)d_2}\left|\frac{(n_r-1)^2 - 4pn_r}{n_r(n_r^2-1)}\right|\right), \tag{1.79b}$$

showing a direct relation between the errors on the optical constant and the variances associated to any noise source introduced by the system [8].

We proceed to analyse some of the possible error sources, and the way they impact results.

THz field ampitude variations

We start the analysis by considering the variations in amplitude of THz radiation, for it we assume a normal probability distribution. Errors in radiation amplitude can be random or systematic. Generally, random errors happen in a short time span whereas systematic errors are visible only when the time scale is long enough. We can express the amplitude-related variances in the optical constant as:

$$s_{n_r,E}^2(\omega) = \left(\frac{c}{\omega d_2}\right)^2\left(\frac{A_s(\omega)}{|E_s(\omega)|^4} + \frac{A_{ref}(\omega)}{|E_{ref}(\omega)|^4}\right) \tag{1.80a}$$

$$s_{k,E}^2(\omega) = \left(\frac{c}{\omega d_2}\right)^2\left(\frac{B_s(\omega)}{|E_s(\omega)|^4} + \frac{B_{ref}(\omega)}{|E_{ref}(\omega)|^4} + \left(\frac{n_2(\omega)-1}{n_2(\omega)+1}\right)^2\frac{s_{n,E}^2(\omega)}{n_2^2(\omega)}\right) \tag{1.80b}$$

with:

$$A_s(\omega) = \sum_\kappa T^2(E_s(\omega)e^{j\omega\kappa\tau})s_{E_s}^2(\kappa), \tag{1.81a}$$

$$A_{ref}(\omega) = \sum_\kappa T^2(E_{ref}(\omega)e^{j\omega\kappa\tau})s_{E_{ref}}^2(\kappa), \tag{1.81b}$$

$$B_s(\omega) = \sum_\kappa R^2(E_s(\omega)e^{j\omega\kappa\tau})s_{E_s}^2(\kappa), \tag{1.81c}$$

$$B_{ref}(\omega) = \sum_\kappa R^2(E_{ref}(\omega)e^{j\omega\kappa\tau})s_{E_{ref}}^2(\kappa), \tag{1.81d}$$

being $s^2_{E_s}, s^2_{E_{ref}}$ variances in time domain sample and reference signal, κ temporal index, τ sampling interval (thus $\kappa\tau$ time). It is interesting to note the trade-off introduced by d_2: in fact, the variances decrease if the thickness of the sample increase, improving the measure, but also the signal E_s decreases as e^{-d_2}, increasing the value of the variance.

Random errors in sample thickness

The variance in the value of the sample's thickness may stem from random errors from the measurement process or from changes in the properties of the sample, for example it could shrink from dehydration.

For this kind of errors as well, we can assume a normal distribution around a mean value so we write the associated variances in the optical constants as:

$$s^2_{n_r,d_2} = \left(\frac{n_2(\omega) - 1}{d_2}\right) s^2_{d_2}, \tag{1.82}$$

$$s^2_{k,d_2} = \left(\frac{k(\omega)}{d_2}\right)^2 s^2_{d_2} + \left(\frac{c}{n_2(\omega)\omega d_2}\right)\left(\frac{n_2(\omega) - 1}{n_2(\omega) + 1}\right)^2 s^2_{n,d_2}(\omega) \tag{1.83}$$

with $s^2_{d_2}$ sample thickness variance, usually obtained from the statistical distribution of several observations. Again, we observe that an increase in sample thickness gives rise to an improvement in the variance but also results in a weaker signal which, while it may not directly affect $s^2_{n_r,d_2}, s^2_{k,d_2}$, still increases the final variance.

Random errors in sample alignment

We try to keep the sample normal to the THz radiation as to avoid an overly complicated transfer function, specifically we avoid deviating the beam and focusing a lowered THz energy to the detector. Unfortunately, as we place or adjust the position of the sample we most likely obtain a small misalignment, causing difference between the thickness d_2 of the sample and the effective propagation path d_{2_θ}, corresponding to l and l_θ respectively in the following figure:

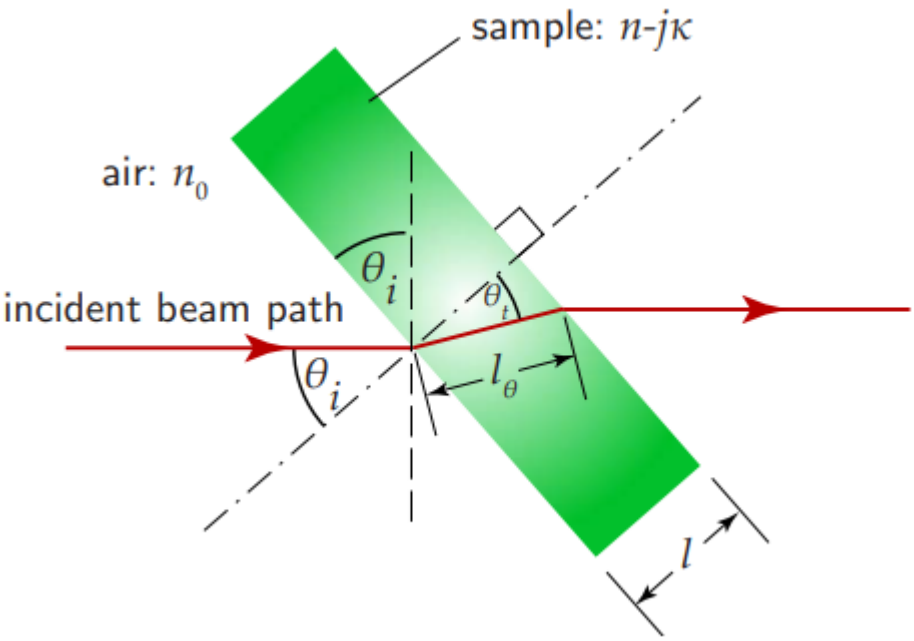

Figure 1.14: Example of sample tilted with respect to the optimal position, orthogonal to the impinging radiation.[25]

For the model we assume a systematic error, a kind of error we observe when the position of the sample is fixed, as opposed to a random one, arising from moving the sample between measures. As it is evident from 1.14, we can express the propagation path as:

$$d_{2_\theta} = \frac{d_2}{cos(\theta_t)}. \tag{1.84}$$

For the angle θ_t we assume small deviations $[-f_\theta, f_\theta]$ around the origin, obtaining the following as the deviation in the propagating path:

$$f_{d_2} = d_2\left(\frac{1}{cos(f_\theta)} - 1\right). \tag{1.85}$$

Finally we write the alignment-related deviations in the optical constants:

$$f_{n_r,\theta} = (n_2(\omega) - 1)\left(\frac{1}{cos(f_\theta)} - 1\right) \tag{1.86a}$$

$$f_{k,\theta} = k(\omega)\left(\frac{1}{cos(f_\theta)} - 1\right) + \frac{c}{n_2(\omega)\omega d_2}\frac{n_2(\omega) - 1}{n_2(\omega) + 1} f_{n,\theta}(\omega). \tag{1.86b}$$

In this case we observe that the variances are not strongly dependent on d_2, in particular $f_{n_r,\theta}$ is not at all dependent on it.

We can now combine all the considered variances to obtain the uncertainties for n and k:

$$u_{n_r}(\omega) = \kappa_p \sqrt{\frac{s^2_{n_r,E_s}}{N_{E_s}} + \frac{s^2_{n_r,E_{ref}}}{N_{E_{ref}}} + \frac{s^2_{n_r,d_2}}{N_{d_2}}} + f_{n_r,\theta}, \tag{1.87a}$$

$$u_k(\omega) = \kappa_p \sqrt{\frac{s^2_{k,E_s}}{N_{E_s}} + \frac{s^2_{k,E_{ref}}}{N_{E_{ref}}} + \frac{s^2_{k,d_2}}{N_{d_2}}} + f_{k,\theta} \tag{1.87b}$$

with $\kappa_p = 1$ for standard uncertainty, $N_{E_s}, N_{E_{ref}}$ number of measures for the sample and reference signals, N_{d_2} number of measures for the sample's thickness [25].

2 | Generation of ultra-short pulses

To obtain THz radiation, it is necessary to work with ultra-short pulses (in the fs range). In the following chapter it will be explained how it is possible to obtain such short pulses. We will start with the description of laser sources emitting femto-second pulses; after that, super-continuum generation, in particular using silica PCF fibers; finally pulse compression using chirped mirrors and grating pairs.

2.1. Femto-second laser sources and mode locking

Let us consider a laser oscillating on a large number of modes N. The modes have the same amplitude E_0 and the difference in frequency between consecutive modes $\Delta\nu$ is constant. If there exists no relation between the modes' phases, then the intensity profile of the output beam, consisting of a random sequence of pulses, each resulting from the sum of the N modes, exhibits a random behaviour. Still the output beam presents some general properties: it has a period of $\tau_p = 1/\Delta\nu$; the pulses have a time duration $\Delta\tau_p \sim 1/\Delta\nu_L$, with $\Delta\nu_L = N\Delta\nu$ total oscillating bandwidth. We can thus say that lasers with large gain bandwidth, such as solid state lasers, can produce ultra-short pulses. It is possible to improve the performance of the described multi-mode lasers by imposing a constant relation between the modes' phases, obtaining a laser that is mode-locked.

Let us now consider a mode-locked laser, and we write the relation between the phase ϕ of one mode l and the previous one $l-1$ as:

$$\phi_l - \phi_{l-1} = \phi, \tag{2.1}$$

with ϕ constant. In general, the spectral envelope of the laser can be approximated as a Gaussian distribution, thus we write the amplitude E_l of a single mode as:

$$E_l^2 = E_0^2 e^{-(\frac{2l\Delta\omega}{\Delta\omega_L})^2 ln(2)}, \tag{2.2}$$

with $\Delta\omega_L$ bandwidth of the spectral intensity.

Figure 2.1: Gaussian distribution of spectral amplitudes of different modes.[20]

The electric field associated to the total wave can be written as:

$$E(t) = A(t)e^{j\omega_0 t}, \tag{2.3}$$

with:

$$A(t) = \sum_{-\infty}^{+\infty} E_l e^{jl(\Delta\omega t+\phi)} \simeq \int E_l e^{jl\Delta\omega t} dl. \tag{2.4}$$

From equation 2.4 we can see that $A(t)$ is proportional to the Fourier transform of E_l. We can now write the intensity of a pulse $A^2(t)$ as a gaussian function of time:

$$A^2(t) \propto e^{-(\frac{2t}{\Delta\tau_p})^2 ln(2)}, \tag{2.5}$$

with $\Delta\tau_p = \frac{0.441}{\Delta\nu_L}$. To conclude the discussion we say that when the laser operates in mode-locking condition, we find that the amplitude of the electric field of the output wave is related to the Fourier transform of the spectral amplitude. As a result, the width of the pulses $\Delta\tau_p$ is proportional to the inverse of the laser spectrum $\Delta\nu_L$, obtaining pulses that are said to be transform limited.

There are two categories of methods to obtain mode locking: passive and active mode-locking. The latter exploits a mode-locking element driven externally, for example a Pockels cell, which provides phase or amplitude modulation[20]. The modulator operates at a frequency $\omega_m = 2\pi/\tau_p$ which corresponds to the spacing between modes.

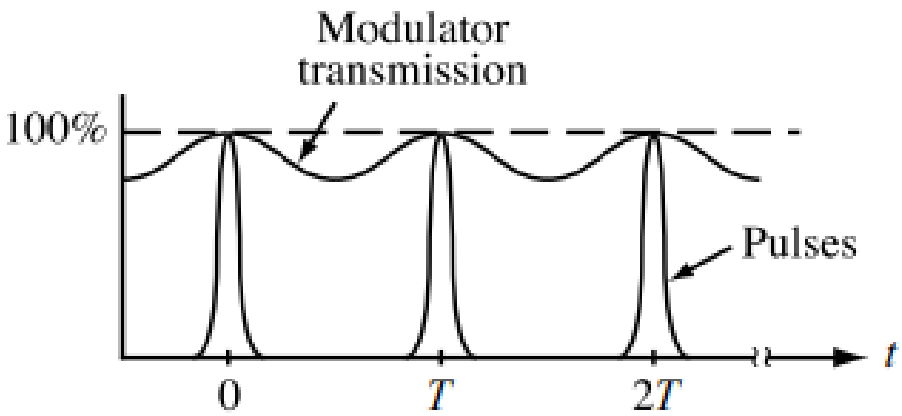

Figure 2.2: Modulator transmission. The resulting pulses are centered around the peaks of the modulator transfer function.[20]

The result is that the radiation is shortened when passing through [23].

Passive mode-locking, instead, exploits non-linear optical effects such as saturation of a saturable absorber or refractive index change of some non-linear materials. In this case it will be the pulse itself that modulates the intra-cavity loss, which will in turn modulate the pulse. For mode-locking, it is necessary that intra-cavity losses reduce with increasing intensity, which is the reason why we can use saturable absorber: their absorption decreases with intensity. When their absorption, l in the following picture, drops below the gain then we obtain a mode-locked pulse.

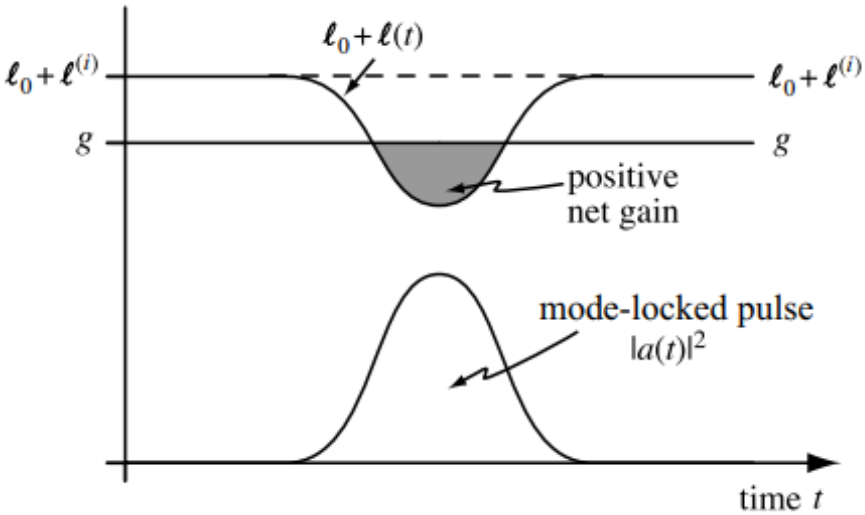

Figure 2.3: Fast saturable absorber mode-locking. Mode-locking condition is met when absorption drops below the gain line, considered constant.[20]

Many lasers now operate in mode-locking condition, some examples include semiconductor lasers, solid-state lasers and dye lasers [20, 23]. In the following section we will analyse a particular kind of solid-state lasers capable of providing ultra-short pulses: fiber lasers.

2.1.1. Fiber lasers

The active medium of a fiber laser is most commonly a Silica fiber doped with a rare Earth element such as, for example, erbium, ytterbium and neodymium. The pump beam comes from laser diodes and propagates longitudinally in the fiber, guided by the core or by an inner cladding. In a conventional fiber the dimension of the pump and laser beam, respectively w_p and w_0, is close to that of the radius of the core. Since the threshold pump power P_{th} is proportional to $\sqrt{w_p^2 + w_0^2}$, we are able to obtain a P_{th} as low as below $1mW$; we can hence expect to obtain lasing activity from active media with very short lifetime τ.

To obtain high power at the output, it is necessary to employ high-power diode lasers, which however do not have the necessary beam quality for efficient pumping. To solve the problem, a particular fiber structure is employed so to allow what is called cladding pumping:

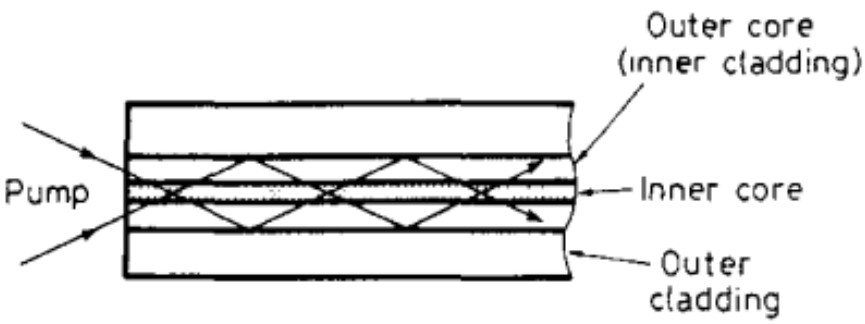

Figure 2.4: General structure of fiber used for cladding pumping.[20]

In this particular fiber, the inner core is surrounded by a first cladding having lower refractive index, referred to as inner cladding or outer core, which is in turn surrounded by cladding having lower refractive index. The beam coming from the diode laser is then launched into the inner cladding so that the quality requirement for the beam becomes relaxed. Given that the core's refractive index is higher, the light is progressively absorbed into it as it propagates through the cladding, with an effective absorption coefficient dependent on the ratio between the inner cladding and the core, both of which, together with the length of the fiber, must be chosen accordingly [20].

2.1.2. Laser RIN

Intensity noise in a solid state laser arises from pump fluctuations and cavity misalignments. These are short term fluctuations. In addition, long terms fluctuations of power are present and are caused by degradation of the optical components of the laser and thermal misalignment of the laser cavity [20]. The optical intensity noise of a system depends on power, so it is usually normalised by the total optical power. The result is called relative intensity noise (RIN), which is indeed defined as the ratio between the noise power spectral density and the total power. To characterise the RIN, it is necessary to use a wideband photodetector, an amplifier and a RF spectrum analyser, also the laser needs to be operated in continuous mode. If intensity noise were absent, the RF analyser would only show a DC component. Instead, the fluctuations in optical power cause fluctuations in the photocurrent of the photodetector; the spectrum analyser then computes the spectral density of the photocurrent fluctuations. Since the electrical power P_{el} at the output of the photodiode is proportional to the square of optical power P_{opt} at its input, we can write the RIN as:

$$RIN = F\left\{\frac{<(P_{opt} - P_{opt,avg})^2>}{P^2_{opt,avg}}\right\}, \tag{2.6}$$

with F Fourier transform.

Equation 2.6 can also be rewritten as:

$$RIN = \frac{S_P(\omega)}{R^2 P_{opt,avg}^2}, \tag{2.7}$$

where $R^2 P_{opt,avg}^2$ is the average signal electrical power, $S_P(\omega)$ is the power spectral density of the electrical noise as measured by the spectrum analyser [17].

2.2. Generation of supercontinuum radiation

In order to effectively generate THz radiation, it is necessary to obtain light pulses having duration in the order of femto-seconds. It is also necessary to broaden the spectrum of the generating beam. One possible way to do this is using a photonic crystal fiber to obtain supercontinuum generation.

Photonic crystal fibers allow strong guidance within their core through a pattern of small holes distributed in their cladding region, running along their entire length, generating the effect of refractive index difference or photonic bandgap effect. The holes achieve large refractive index modulation by changing the fiber's dispersion. In order to select the wavelength of the electromagnetic radiation to guide through the PCF, one needs to vary the patterning and parameters of the air holes. These key structural parameters are: the hole diameter d, the center to center hole spacing (pitch) Λ, the core diameter d_{core} and the number of hole rings.[15]

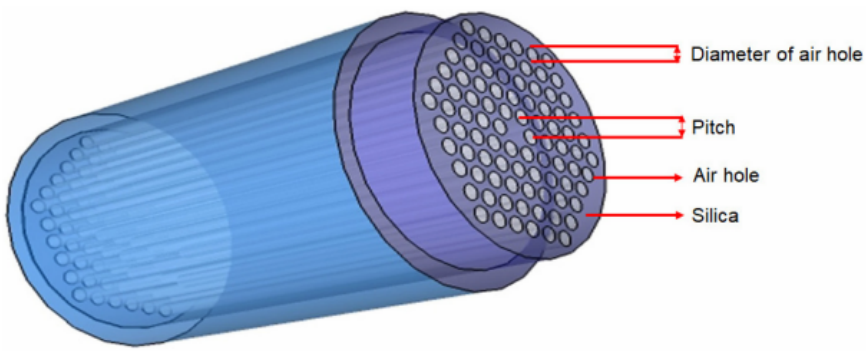

Figure 2.5: General schematic of a silica photonic crystal fiber. In the image the key structural parameters are highlighted. [15]

Supercontinuum generation in optical fiber is obtained thanks to simultaneous action of

both linear and nonlinear effect. For simplicity, let us consider each effect's influence on radiation separately. The first one we consider is a linear one: dispersion.

Dispersion happens because the effective index of the guided mode varies with frequency, as a result of material and waveguide contributions. Dispersion influences both group velocity and phase velocity of the radiation propagating in the fiber. The group velocity dispersion (GVD) β_2 is the coefficient of the Taylor series expansion's second term of the propagation constant. When $\beta_2 > 0$ we are in normal dispersion regime, instead when $\beta_2 < 0$ we are in anomalous dispersion regime. If no non-linearities are present, the spectrum of the propagating radiation will broaden in a way that is independent from the sign of β_2; however, in presence of non-linearities, the sign of the GVD dispersion greatly influences the propagation dynamics.

Now we consider self and cross-phase modulation, SPM and XPM respectively, nonlinear effects related to the Kerr effect. The time dependent intensity of the propagating pulse $I(t)$ causes a variation of the local refractive index of the fiber $\Delta n = I(t)n_2$, causing a time dependent phase delay to a single pulse (SPM) or to co-propagating pulses (XPM). If we consider a temporally symmetric single pulse, SPM will determine a spectral broadening that is also symmetric and will not change the time domain envelope of the pulse. If we consider the simultaneous interaction of SPM and normal dispersion, we obtain a pulse which experiences broadening both in time and frequency domain.

The interplay of anomalous dispersion and SPM, instead, leads to the generation of solitons which introduce propagation effects characteristic of soliton dynamics. Initially, there will be a phase with spectral broadening and temporal compression. After that, because of the instability of the solitons generated, Raman scattering and higher order dispersion will cause their decay into lower amplitude sub-pulses. This process is also referred to as soliton fission and it usually happens at the point in the fiber where the soliton reaches its maximum bandwidth; evidently, choosing a length for the fiber which is just a bit shorter than the fission length is the basis of soliton effect compression technique. Another important effect to consider, other than soliton fission, is the generation of a dispersive wave, that happens when a soliton propagate close to the zero dispersion wavelength regime (ZDW). If the individual solitons bandwidth overlap the Raman gain, it is possible to observe self-frequency shift, even in presence of perturbation by dispersive wave generation. Moreover, GVD matching and XPM between solitons and dispersive waves induces trapping effects that further contribute to spectral broadening [2].

2.2.1. Silica PCF for supercontimuum generation

If we want to generate supercontinuum radiation it is important to choose medium with the right characteristics. In case of PCF, or silica fibers in general, here are the most important parameters to consider: dispersion of the fiber; Kerr intensity-dependent refractive index n_2; effective area of the fiber mode; material-dependent time-delayed Raman response; spectral transparency of the material; power handling capability of the material.

Silica is an optimal material for supercontinuum generation. It presents very low attenuation in the wavelength $1300 - 1600nm$, which however increases for shorter wavelengths, because of Rayleigh scattering, and for longer wavelengths, because of phonon absorption. In the following image it is presented the behaviour in silica of refractive index n, group index n_g and GVD $D = \frac{-\lambda}{c}\frac{d^2n}{d\lambda^2}$ with respect to the wavelength of the propagating radiation:

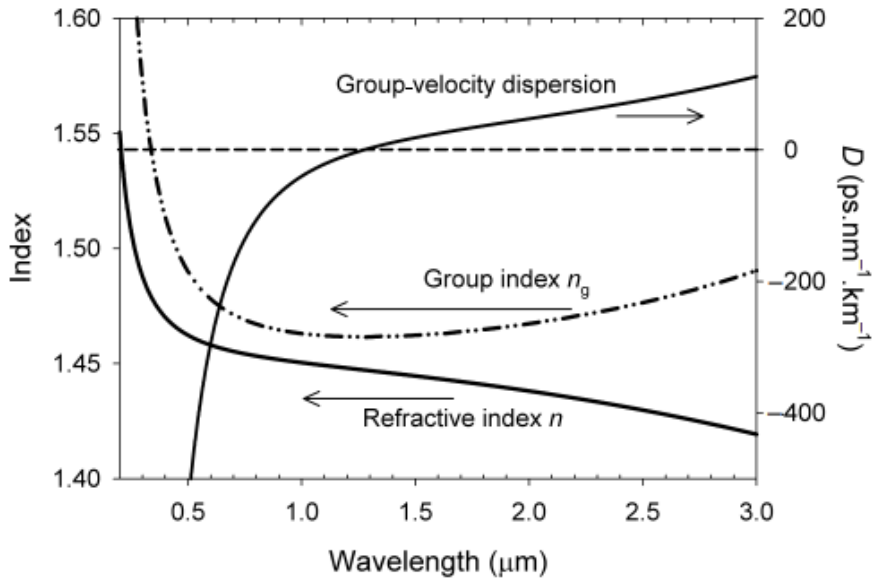

Figure 2.6: Group index, refractive index and group velocity dispersion D for bulk silica, plotted with respect to the wavelength of radiation propagating through it.[2]

The GVD D crosses 0 at $1300nm$; it is positive, signifying anomalous dispersion, for longer wavelengths and negative, signifying normal dispersion, for shorter wavelengths. Silica Kerr response is low, however its broad Raman gain, long interaction lengths and high confinement compensate for it.

The advantage offered by PCFs with respect to conventional silica optical fibers is the possibility to customise their dispersion curves by changing the geometry of their struc-

ture, namely by varying the diameter of the air holes present in the cladding, other than the diameter of the core $d_{core} = 2\Lambda - d$.

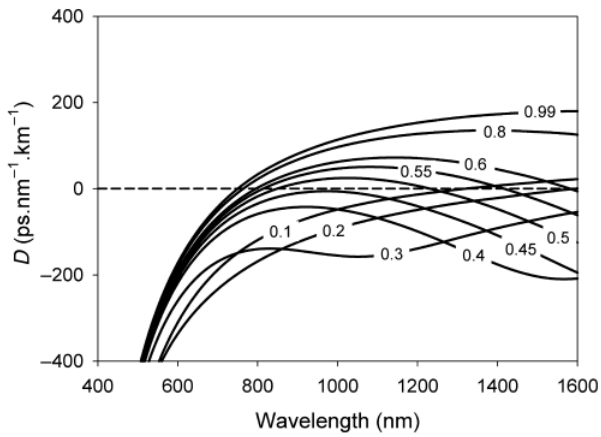

(a) D curves with respect to wavelength for a fixed core diameter of $2\mu m$ but different d/Λ.[2]

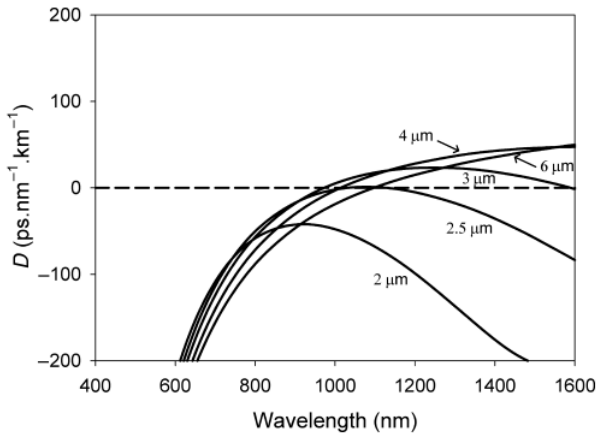

(b) D curves with respect to wavelength for fixed $d/\Lambda = 0.4$ but different core diameter.[2]

2.3. Dispersion and compensation

The laser pulses then propagate through the set up and experience dispersion, which extends their time duration. The electric field associated to the pulses can be written, in the frequency domain, as:

$$E(\omega) = |E(\omega)|e^{-j\psi(\omega)}, \tag{2.8}$$

where, for simplicity, we do not consider the spatial dependence of the field.

To obtain the expression of the electric field in the time domain, it is necessary to compute the inverse Fourier transform of 2.8; for our purposes we consider a small interval $\Delta\omega$

centered around $\tilde{\omega}$, obtaining:

$$E_{\tilde{\omega}}(t) = \frac{1}{2\pi}\int_{\tilde{\omega}+\frac{\Delta\omega}{2}}^{\tilde{\omega}-\frac{\Delta\omega}{2}} |E(\omega)|e^{-j\psi(\omega)}e^{j\omega t}d\omega. \tag{2.9}$$

If we consider $\Delta\omega$ small enough, we can linearise the phase term:

$$\psi(\omega) = \psi(\tilde{\omega}) + \left.\frac{\partial\psi}{\partial\omega}\right|_{\tilde{\omega}}(\omega - \tilde{\omega}) \tag{2.10}$$

By inserting 2.10 into 2.9 we get:

$$E_{\tilde{\omega}}(t) = \frac{1}{2\pi}e^{j(\tilde{\omega}t-\psi(\tilde{\omega}))}\int_{\tilde{\omega}+\frac{\Delta\omega}{2}}^{\tilde{\omega}-\frac{\Delta\omega}{2}} |E(\omega)|e^{-j(\omega-\tilde{\omega})}e^{j(t-\frac{\partial\psi}{\partial\omega}\big|_{\tilde{\omega}})}d\omega. \tag{2.11}$$

We know that $E_{\tilde{\omega}}$ will be maximum when $t = \frac{\partial\psi}{\partial\omega}\big|_{\tilde{\omega}}$, as a result we can say that:

$$\tau_g(\tilde{\omega}) = \left.\frac{\partial\psi}{\partial\omega}\right|_{\tilde{\omega}}, \tag{2.12}$$

being τ_g the group delay.

To account for dispersion, we rewrite equation 2.12 as centered in the carrier frequency and we expand it to third order terms:

$$\tau_g(\omega) = \tau_g(\omega_0) + \left.\frac{\partial^2\psi}{\partial\omega^2}\right|_{\omega_0}(\omega-\omega_0) + \frac{1}{2}\left.\frac{\partial^3\psi}{\partial\omega^3}\right|_{\omega_0}(\omega-\omega_0)^2 = \tau_{g0} + D_2(\omega-\omega_0) + \frac{1}{2}D_3(\omega-\omega_0)^2, \tag{2.13}$$

where D_2 is the second order dispersion and D_3 is the third order dispersion.
If the laser pulse propagates in a linear optical material of length L, then its phase term can be written as $\psi(\omega) = k(\omega)L = \frac{\omega L}{c}n(\omega)$, which in turns allow us to rewrite the second order dispersion D_2 as:

$$D_2 = \frac{\partial^2\psi}{\partial\omega^2} = \frac{L\lambda^3}{2\pi c^2}\frac{\partial^2 n}{\partial\lambda^2}. \tag{2.14}$$

Following the same logic, we rewrite D_3:

$$D_3 = \frac{L\lambda^4}{4\pi^2c^3}(3\frac{\partial^2 n}{\partial\lambda^2} + \lambda\frac{\partial^3 n}{\partial\lambda^3}). \tag{2.15}$$

In order to correct the dispersion effect without modifying the amplitude of the electric

field, we need to add a phase term to equation 2.8 by means of a pulse compressor. The dispersion at the output of the compressor is: $D_{nOUT} = D_{nIN} + D_{nC}$, thus we obtain a dispersion equal to zero by imposing $D_{nC} = -D_{nIN}$ [10] .

Now we report some possible solutions to reduce dispersion effects on laser pulses.

Chirped mirrors

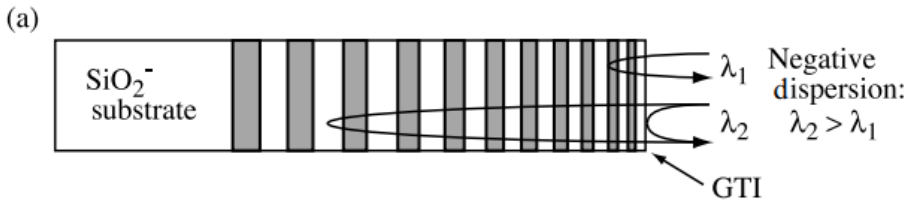

Figure 2.7: General structure of a chirped mirror with negative dispersion D.[23]

A chirped mirror consists of numerous dielectric layers having different thickness, resulting in different λ_B for each layer, stacked on a substrate (for example SiO_2). We call λ_B Bragg's wavelength and we define it as the particular wavelength that experiences a $\pi/2$ phase-shift when passing through a layer of a reflector; it is computed as: $\lambda_B = 2(n_H d_H + n_L d_L)$.

The idea behind chirped mirrors is that different frequencies penetrate to different depths before being reflected, resulting in frequency dependent delay. In order to provide a negative dispersion, it is necessary to choose chirped mirrors having dielectric layers with higher λ_B the closer they are to the substrate. [23]

Grating pairs

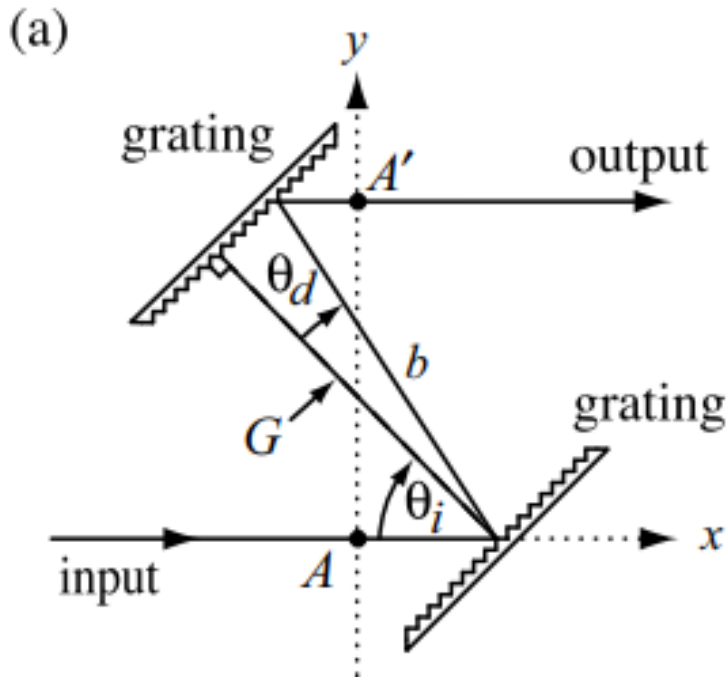

Figure 2.8: General scheme depicting the working principle behind parallel grating pair.[23]

To compute the dispersion introduced by a grating pair, let us consider an input beam impinging on the first grating with angle θ_i. The input beam will be diffracted of an angle θ_D which depends on frequency; then, after diffracting on the second grating, all the output rays will be parallel to the input beam, regardless of their frequency. To prevent spatial separation of the beam's components, one can add a mirror to reflect the output rays: these will recombine into a single collimated beam, travelling in the opposite direction with respect to the original one. It can be demonstrated that the dispersion of this particular structure is:

$$D_2 = \frac{\partial^2 \psi}{\partial \omega^2} = \frac{m^2 \lambda^3 b}{\pi c^2 d^2 cos^2(\theta_D)}, \tag{2.16}$$

with m diffraction order, b distance traveled by the beam, d periodicity of the grating ruling. The third order dispersion D_3 of grating pairs always has sign opposite to the one of D_2. If the dispersion we need to compensate comes from a material with D_2, D_3 having the same sign, such as most transparent materials, it is impossible to use grating pairs to compensate simultaneously for both effects [23].

3 | Experimental results

In this chapter it will be described the experimental setup that was implemented to generate and detect THz radiation. It will be divided into two main sections: one related to the setup used for generation via optical rectification and one to the setup used for detection via electro-optical sampling. Also, attention will be put on all the steps taken to ensure good operation.

3.1. Yb fiber laser and photonic crystal fiber

The laser used in the experimental setup is the OneFive aeroPULSE-FS20, a Yb doped fiber laser emitting ultra-short pulses at $\lambda = 1030nm$; The duration of the single pulses is tunable and can be chosen within the range $0.5 - 3ps$. The laser can be operated in continuous mode or choosing a repetition rate between $200kHz$ and $50MHz$. The maximum average output power is $20W$.

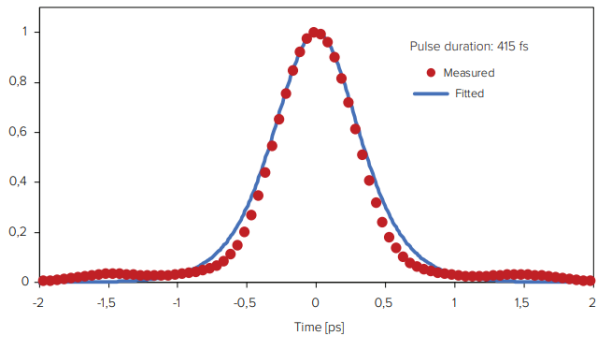

(a) Autocorrelation of aeroPULSE FS20.

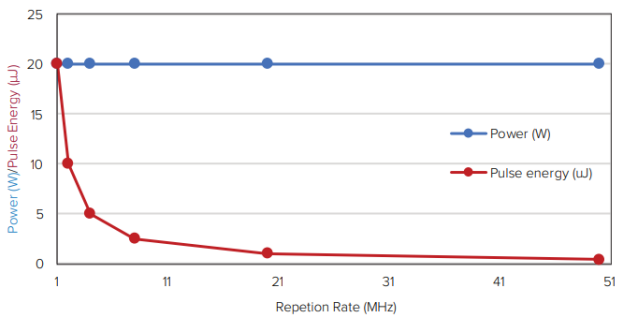

(b) Output power vs repetition rate.

[12]

In order to maximise THz generation, we chose to operate with maximum power, corresponding to $20W$, and repetition rate of $25MHz$, a choice that will be justified in the following sections; also we set $\beta_2 = 28.2\%, \beta_3 = 41.1\%$, indicating group velocity and third order dispersion respectively.

The laser beam is redirected towards the PCF (photonic crystal fiber), using two high reflectivity mirrors, and focused into its core thanks to a lens having diameter $d = 25.4mm$ and focal length $f = 30mm$; a second identical lens, placed $30mm$ after the PCF, collimates the laser beam. In order to minimise power loss and to ensure good quality of the beam, it is necessary to make sure that the laser is perfectly coupled to the fiber; for this purpose we observed the shape and dimension of the beam right after the fiber using a camera and we monitored power loss using a power meter. In the end we were able to limit power loss to 20% and to obtain a reasonably shaped beam.

As explained in 2.2.1, the fiber causes a broadening of the spectrum of the radiation, which was verified using a spectrometer:

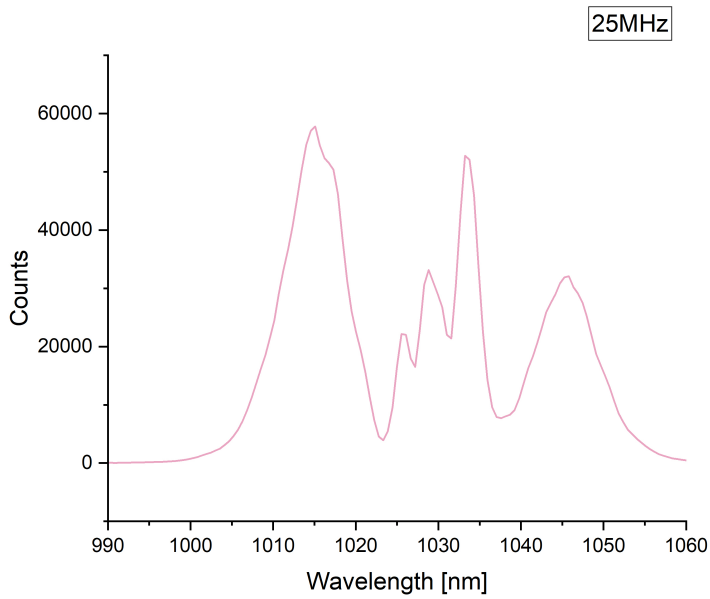

Figure 3.1: Broadened spectrum of laser radiation with rr=25MHz.

We can compare the previous image with the following one, representing the broadening of the spectrum of the laser's radiation when a repetition rate of $50MHz$ is selected:

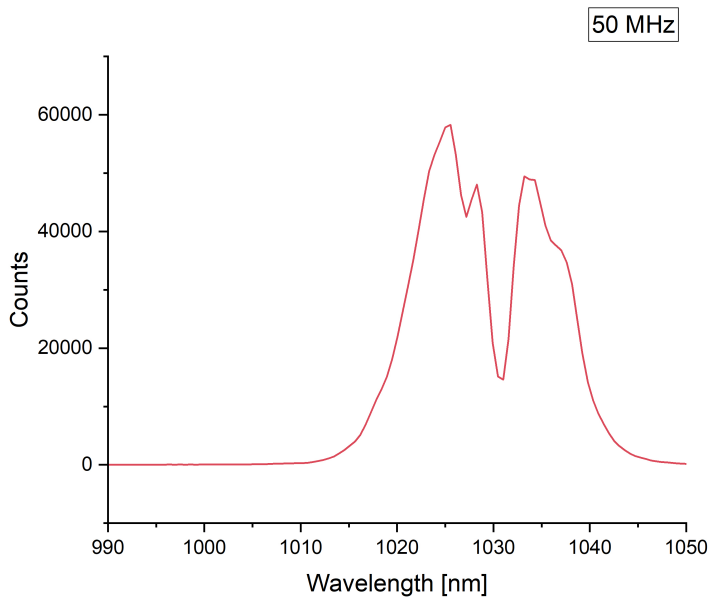

Figure 3.2: Broadened spectrum of laser radiation with rr=50MHz.

With an increased repetition rate, but a fixed average power, pulses are less intense: this

means that the nonlinear effects induced by the fiber are less pronounced, which prompted us to choose to work at $25MHz$.

3.2. Auto-correlation for pulse duration

After checking the broadening of the spectrum of the laser pulses, we decided to check their temporal duration too. Since it is not possible to measure the duration of ultra-short laser pulses using electronics, we used an auto-correlator.

The following image represents the obtained measure of the pulses' auto-correlation:

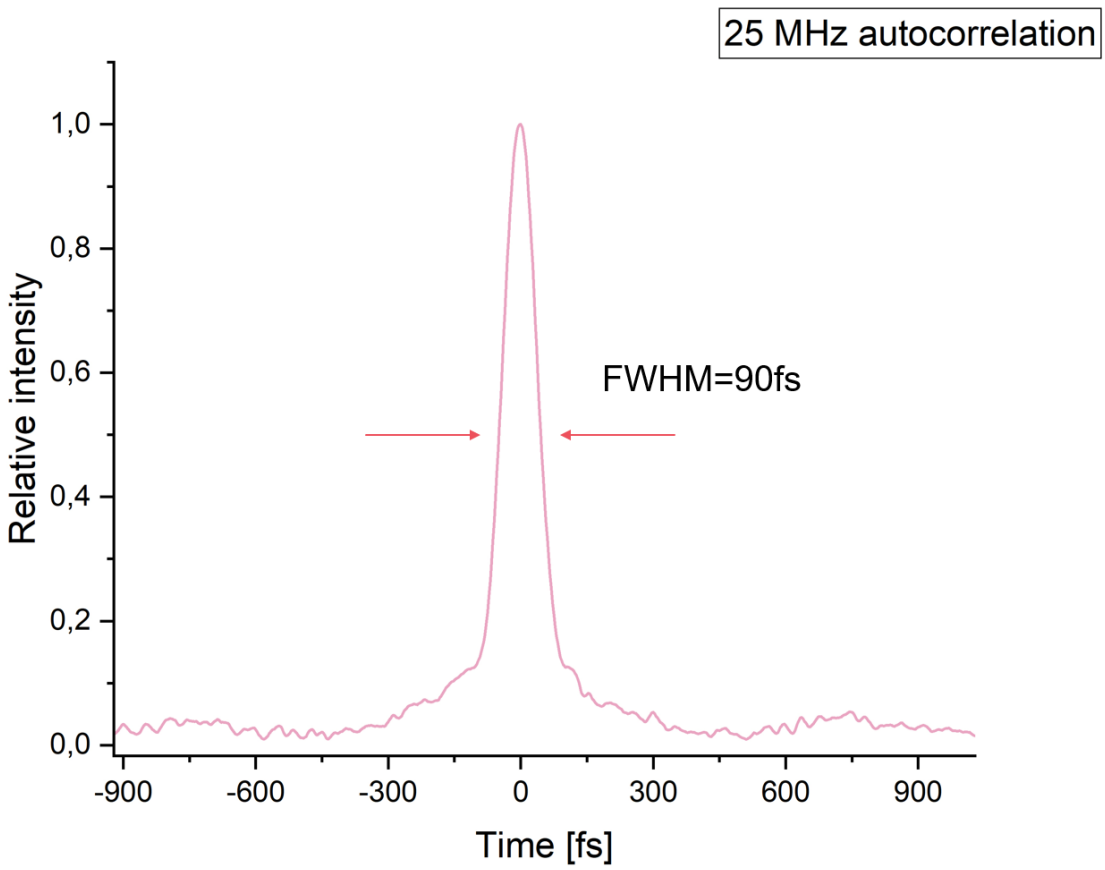

Figure 3.3: Auto-correlation of shortened laser pulses. The FWHM is $90fs$, indicating a pulse duration of $60fs$.

Its full width half maximum (FWHM) is about $90fs$, indicating a duration of the pulses of about $60fs$. For comparison, the following image represents the auto-correlation of the laser's pulses when the repetition rate is $50MHz$:

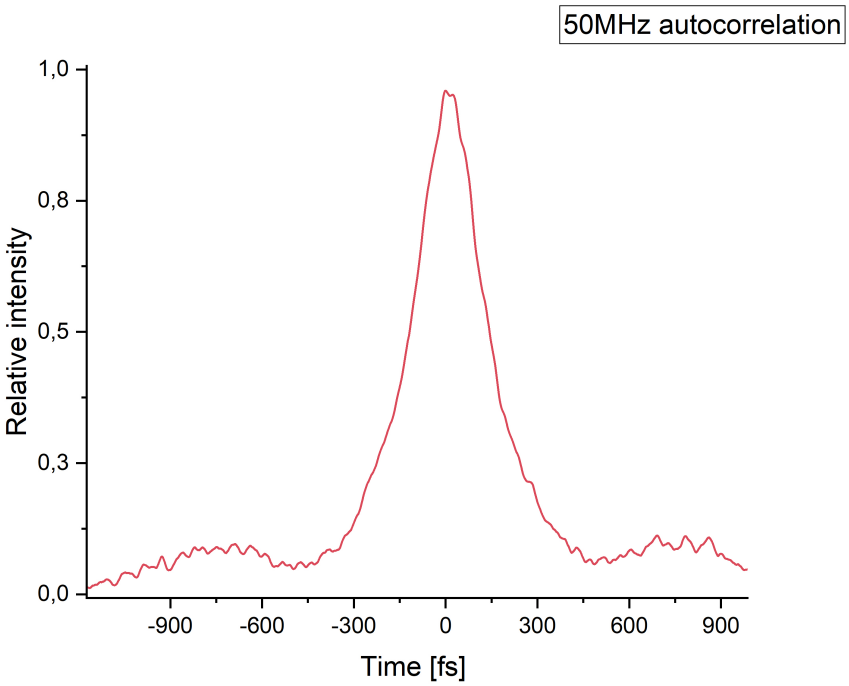

Autocorrelation of laser's pulses when rr=50MHz

Figure 3.4: .

Again it appears evident how the choice to use a repetition rate of $25MHz$ is the better one as the final pulses are shorter.

3.3. Experimental setup used for generation of THz radiation

The following image represents the total experimental setup implemented:

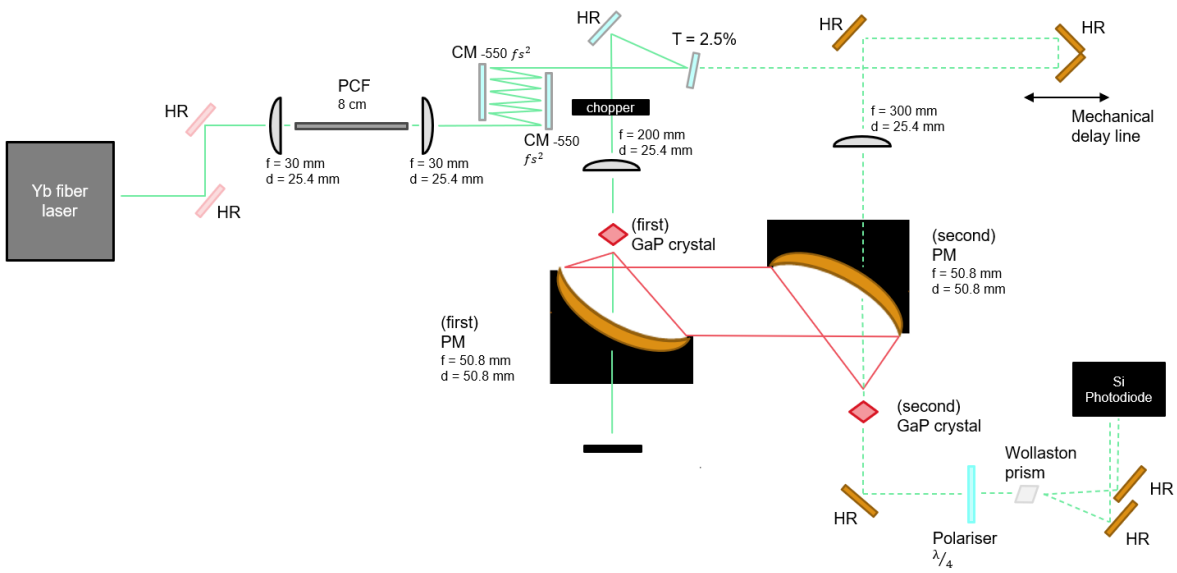

Figure 3.5: Complete experimental setup. CM stands for Chirped Mirrors, HR for High reflectivity, PCF for photonic crystal fiber, PM for parabolic mirror, T is the transmission coefficient of the output coupler.

In this section its first part will be discussed, up until the second parabolic mirror, neglecting the delay line, which will be discussed later.

In order to counterbalance the dispersion effects introduced on the pulses by the lens, output coupler and crystal, the beam is made to reflect on a couple of chirped mirrors (see 2.3), specifically five times on each mirror, introducing a chirp of $-550fs^2$. Next the beam is split in two by an output coupler having transmission coefficient $T = 2.5\%$: one to be used for THz generation and the other to be used as a probe for detection;

As it is explained in 1.1, the THz electric field strongly depends on the intensity of the generating radiation, as normally expected when dealing with non-linear effects; as a result, in order to obtain the best possible efficiency in the generating process, we made sure to maximise the intensity of the radiation impinging on the crystal. This is practically achieved by using the beam reflected by the output coupler and subsequently focusing it on the crystal, which was made using a lens having diameter $d = 25.4mm$ and focal length $f = 200mm$. The point corresponding to the actual focus of the lens, in which we placed the generating GaP crystal (110), was found by observing the dimension of the beam in a spatial interval around the lens' nominal focus with a camera: the optimal point was found to be at a distance of $215mm$ from the lens, and the minimum dimension recorded for the beam was $D4\sigma = 157\mu m$. In the following image it is possible to compare the

profile of the beam with and without lens:

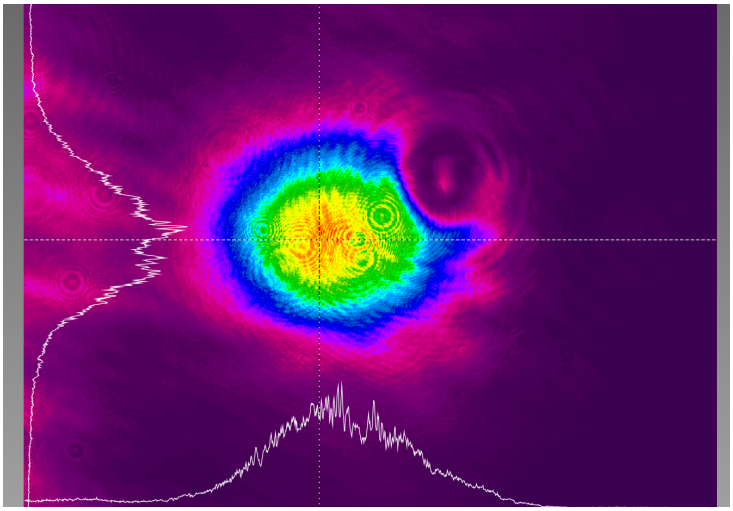

Figure 3.6: Beam profile without lens.

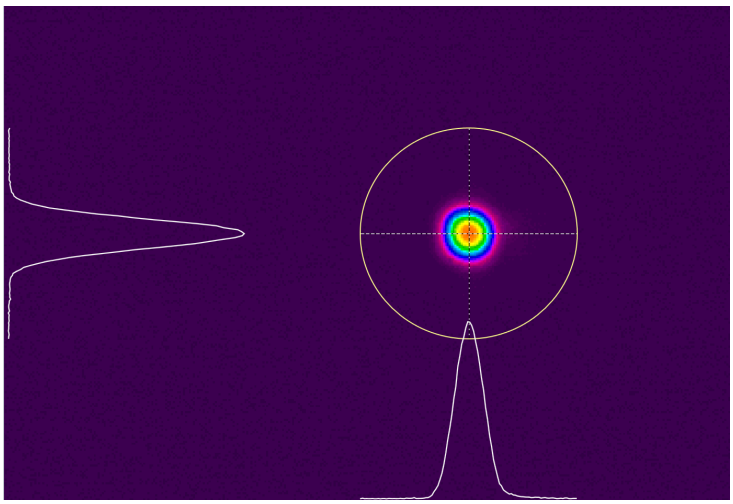

Figure 3.7: Beam profile with lens.

It is explained in 1.1.3 that THz radiation diverges very quickly, thus, to collect as much radiation as possible after the crystal, a gold coated paraboloid, having dimension $d = 50.8mm$ and focal length $f = 50.8mm$, is used; the parabolic mirror is placed so that the crystal is in its focus, resulting in a collimated THz beam. Since we did not need it anymore, and to prevent saturation during the detection phase, we discarded the pump using a hole present at the center of the mirror. The collimated radiation is then collected and focused on another GaP crystal (110) by a second parabolic mirror, identical to the first one, as required for detection via electro-optical sampling.

Again, given the nonlinear nature of the phenomenon to excite and the tendency of THz radiation to diverge, it was particularly important to identify the actual position of the focus of the second parabolic mirror. Since this time we were unable to use the camera, we used a Golay cell (see A.1) to detect the radiation of interest and, in particular, to pinpoint the distance from the paraboloid corresponding to the maximum of the signal.

The detection setup was implemented in the following way:

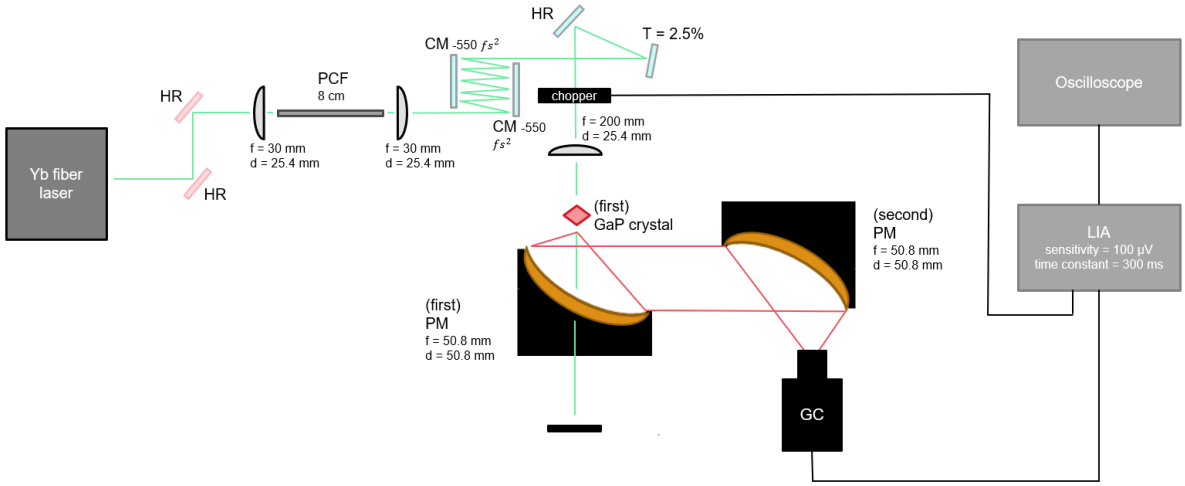

Figure 3.8: Setup to measure THz using the Golay cell.

The Golay cell we used needed its input signal modulated at $18Hz$, so a chopper was used to modulate the laser beam. The cell was placed in the focus of the second parabolic mirror and its output connected to the input of a lock-in amplifier (LIA), which received its reference signal from the chopper. The LIA setting used were $100\mu V$ for sensitivity and $300ms$ for time constant. After determining the optimal position for the focus, we proceeded to measure the THz signal with respect to the power of the generating beam, obtaining the following results:

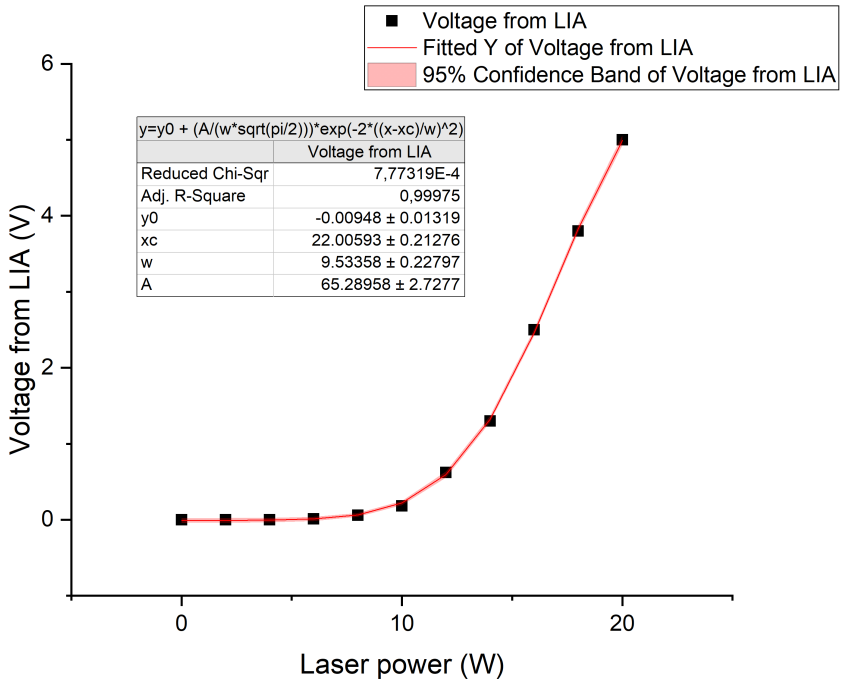

Figure 3.9: Golay output signal versus power of laser beam.

We found that the relation between laser power and output signal is approximated by a Gaussian function; the parameters of the function are reported in the previous image 3.9. Because the cell we used had its entrance window made of diamond, it was receptive to wavelengths ranging from $0.4\mu m$ to $8000\mu m$. To prevent saturation and potential damages, we had to place an attenuator right in front of it: the chosen one slightly attenuated THz radiation while completely blocking other unwanted frequencies.

3.4. Experimental setup for detection via EO sampling

Once we made sure the first part of the setup (see figure 3.5) was working as expected, we started working on detection. For EO sampling we needed THz radiation and a probe, for which we used the beam transmitted through the previously mentioned output coupler. The transmitted beam propagates through a movable delay line, obtained by mounting a retroflecting gold coated prism mirror on a precision motion control linear stage from Kensington laboratories (model: metric 6000-4). It is then focused on the detection GaP crystal (110) by a lens having $d = 25.4mm$ and $f = 300mm$, passing through the hole present at the center of the second parabolic mirror.

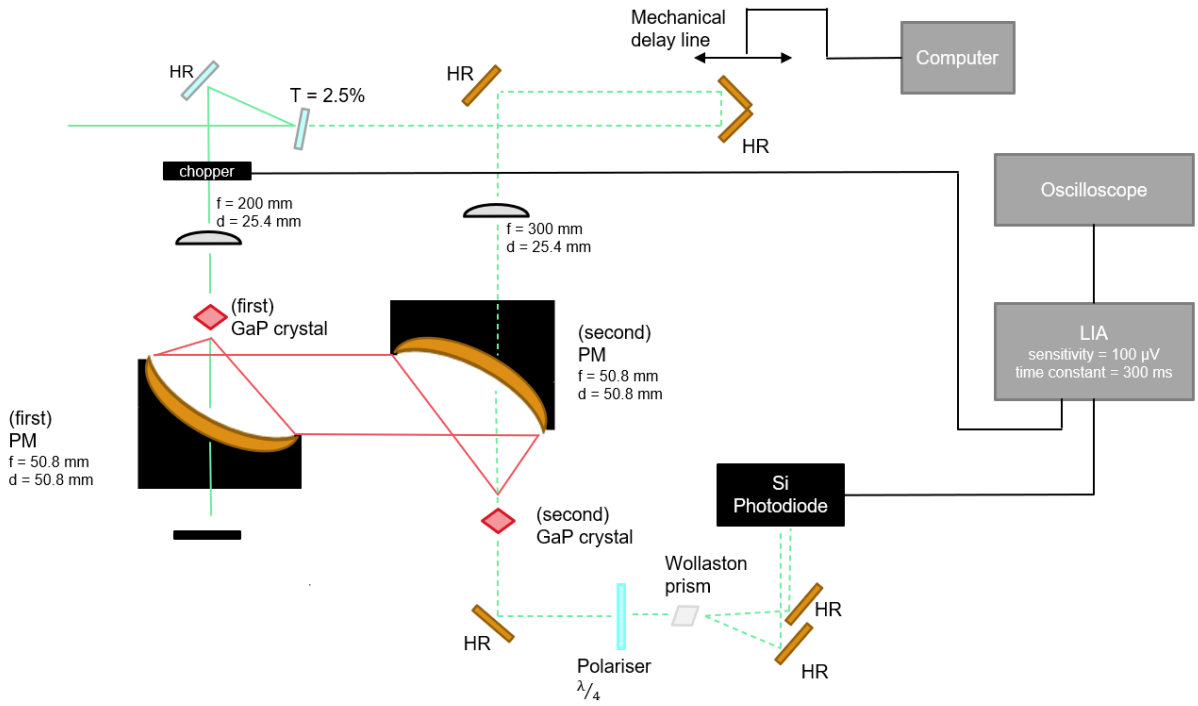

Figure 3.10: Second of the experimental setup, used for EO sampling.

As explained in 1.2.3, EO sampling works best when THz radiation and probe beam are perfectly overlapped while propagating through the detection GaP crystal. Making sure that this condition was verified proved particularly challenging because the camera we were using could not show us THz radiation; to circumvent the problem, we decided to use a scattering glass instead of the generating crystal so that we could obtain a beam approximating THz behaviour. Being now able to use the camera, we placed it in the focus of the paraboloid and then away from it to improve the alignment of probe and scattered radiation and the quality of the parabolic mirror's focusing action; the following pictures show the end results:

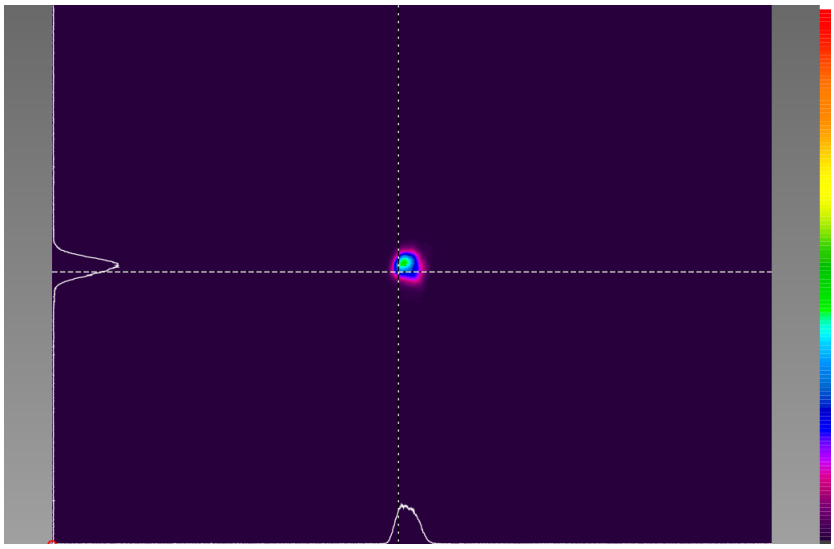

(a) Probe beam out of focus.

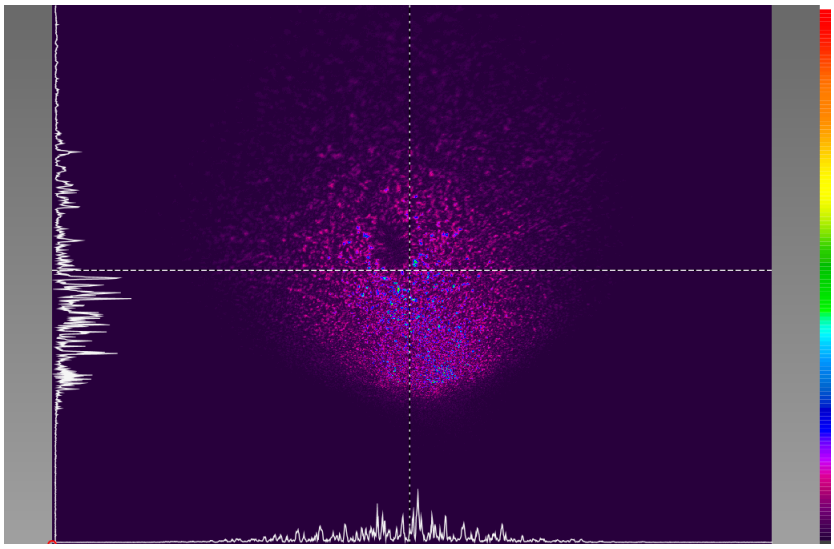

(b) Scattered radiation out of focus.

Figure 3.11: Scattered radiation and probe beam taken separately in the same position out of focus.

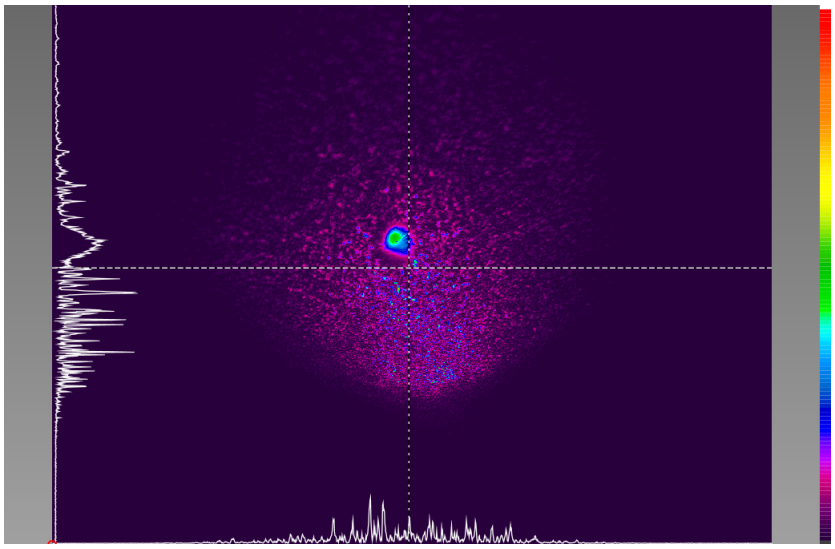

(a) Superposition of scattered radiation and probe beam out of focus.

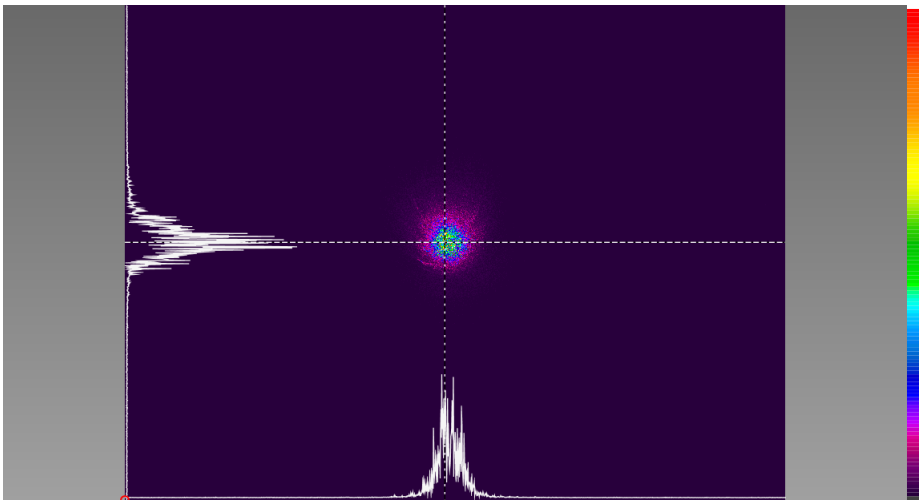

(b) Superposition of scattered radiation and probe beam in focus.

Figure 3.12: Comparison between out of focus and focused superimposed beams.

The probe beam, modulated by its interaction with THz radiation in the crystal (see 1.2), passes through a $\frac{\lambda}{4}$ polariser, then a Wollaston prism. Finally the two resulting beam are directed toward the inputs of a balanced amplified Si photodetector with switchable gain (Thorlabs PDB450A). The photodetector has a damage threshold of $20mW$, so we used a linear attenuator placed between the $\frac{\lambda}{4}$ polariser and the prism.

3.5. Relative intensity noise of the system

Before carrying out a measure of our THz radiation, we decided to characterise the system by computing the RIN of the laser and then the RIN of the radiation right after the PCF,

to also get a measure of the noise introduced by it.

To compute the RIN of our system we used a Si switchable gain detector (Thorlabs PDA36A2) with settings $Gain = 0dB$ and $BW = 12MHz$ and a spectrum analyser (AGILENT E4445A) with a high pass filter at the input, blocking frequencies below $100Hz$. In the following images it is shown the setup used for the RIN measures:

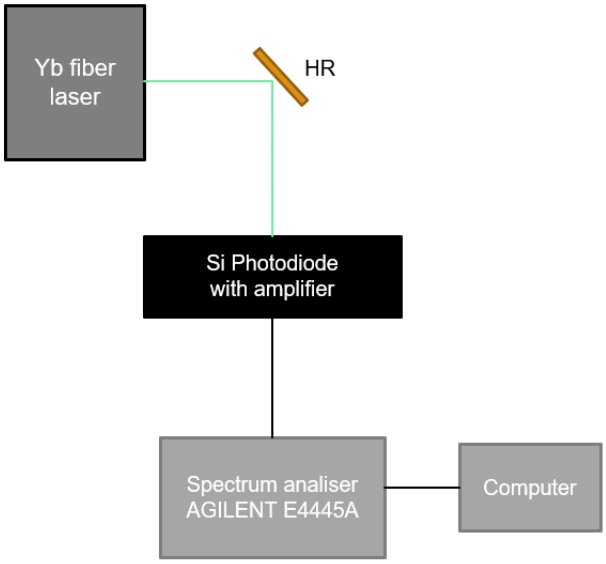

(a) Setup used to measure the RIN before the PCF.

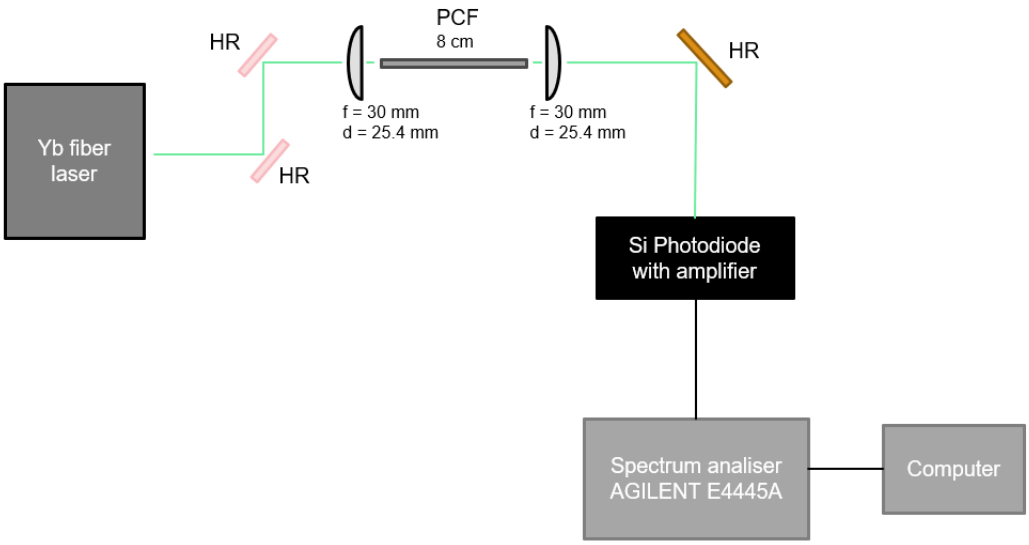

(b) Setup used to measure the RIN after the PCF.

For both measures, we acquired the RIN twice: once without the laser beam, to obtain a

noise floor, and once with the laser beam. As said before, the laser was used in continuous mode at maximum power, consequently we added an attenuator at the input of the photodiode to avoid damaging it or saturating the signal.

In the following image it is possible to compare the RIN with and without the photonic crystal fiber:

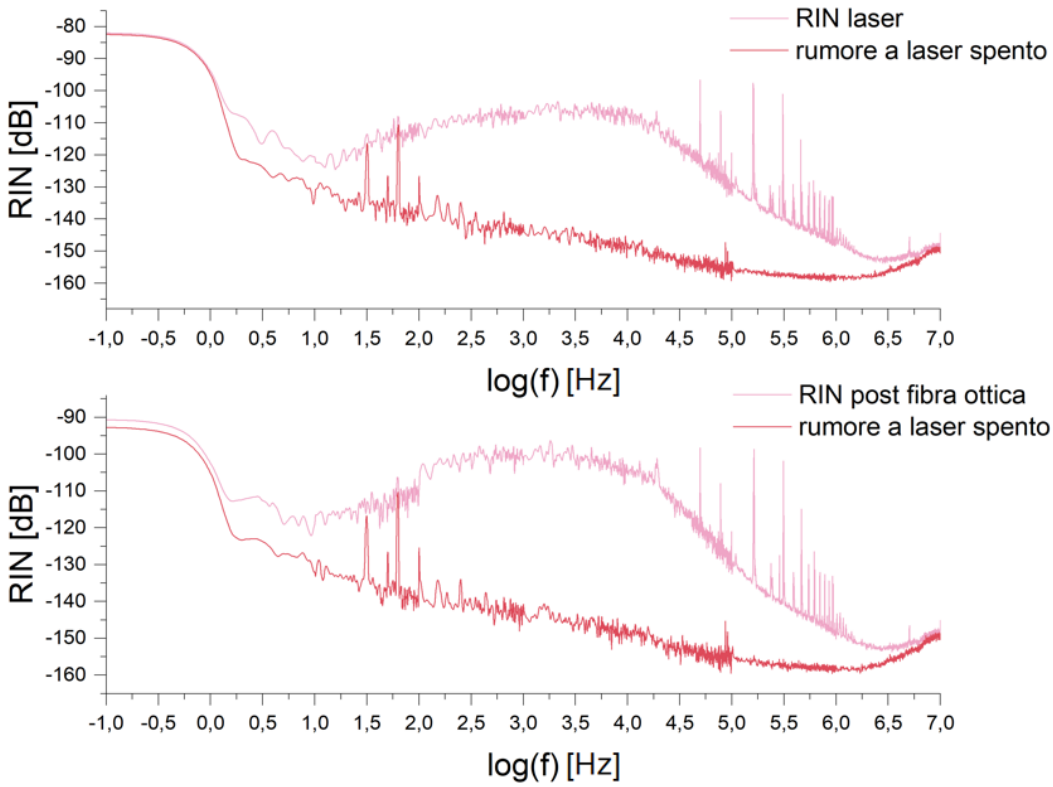

Figure 3.13: Laser RIN before and after PCF.

It can be seen that the fiber adds roughly $20dB$ to the RIN of the system in the frequency range $100Hz - 18kHz$.

3.6. Measures and results

After characterising the noise of the system, we started with the measures. We decided to modulate the generating beam using a chopper, setting the frequency at $5kHz$, and used its output signal as the reference for the lock in amplifier (see A.2). Before starting, it is important to check that the two beams coming out of the Wollaston prism are balanced, so to avoid an offset at the output; for this purpose we prevented THz generation and we observed the signal at the output of the photodetector using the oscilloscope, then we

rotated the polariser until we obtained a null output, signifying identical beams at the input of the balanced photodiode.

The THz measure is obtained by slowly moving the delay line while acquiring the output of the LIA, which receives its input from the photodiode. In particular, the entire operation is coordinated by a matlab script (see B.1): first the linear stage is made to move of $\Delta x = 6\mu m$, referring to the previous point on the linear stage, then a NI usb-6221 DAQ acquires data for $0.1s$ with an acquisition frequency of $1000 samples/s$; finally the average of the acquired data is stored and the process is repeated N times, a number previously set. The script also computes the normalised fast Fourier transform of the data. To improve the quality of the measure it is also possible to make multiple complete acquisitions and then average them.

We now report two different measures. The first one was obtained setting $N = 320$ as the number of steps taken by the linear stage, with a $\Delta x = 6\mu m$. The x-axis represents the position on the linear stage.

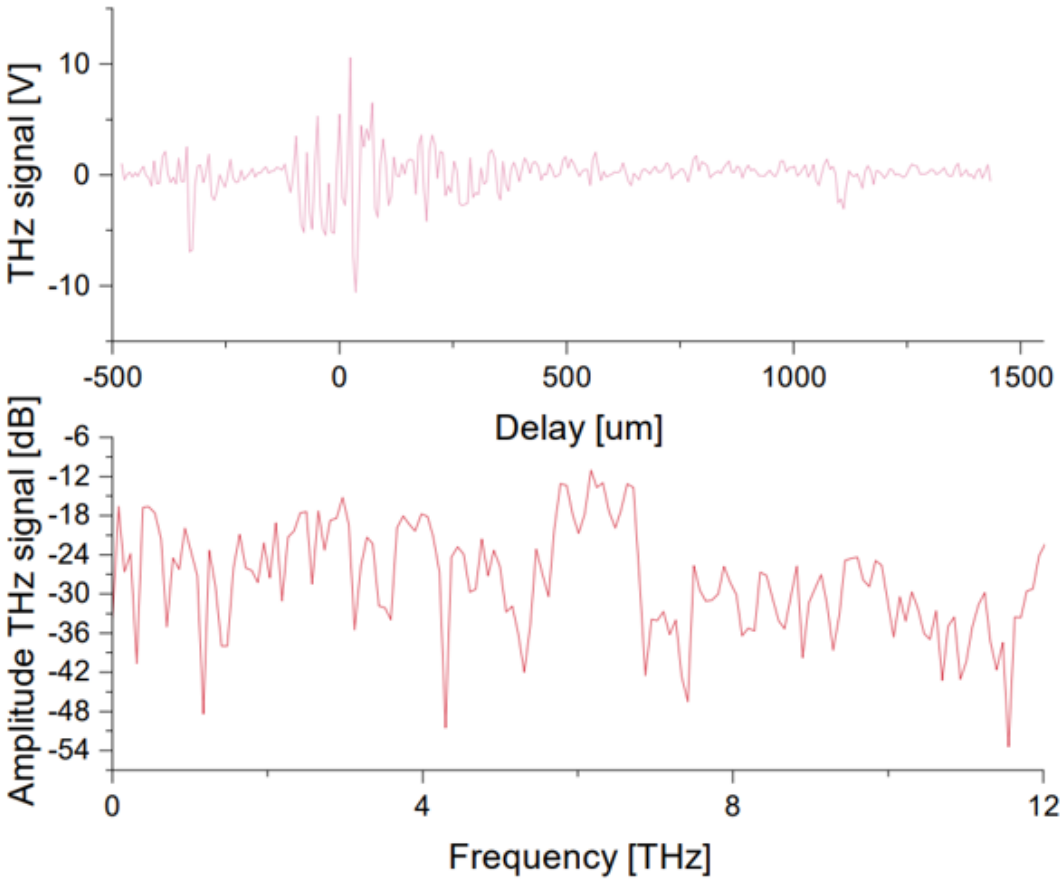

Figure 3.14: THz output signal in time and frequency domain. The considered signal is the tension coming from the LIA in time domain and its fast fourier transform in frequency domain.

The second one was obtained setting $N = 1000$, again with a $\Delta x = 6\mu m$, which was translated to a temporal delay using the formula: $\frac{2\Delta x}{c}$ (for more details see B.1).

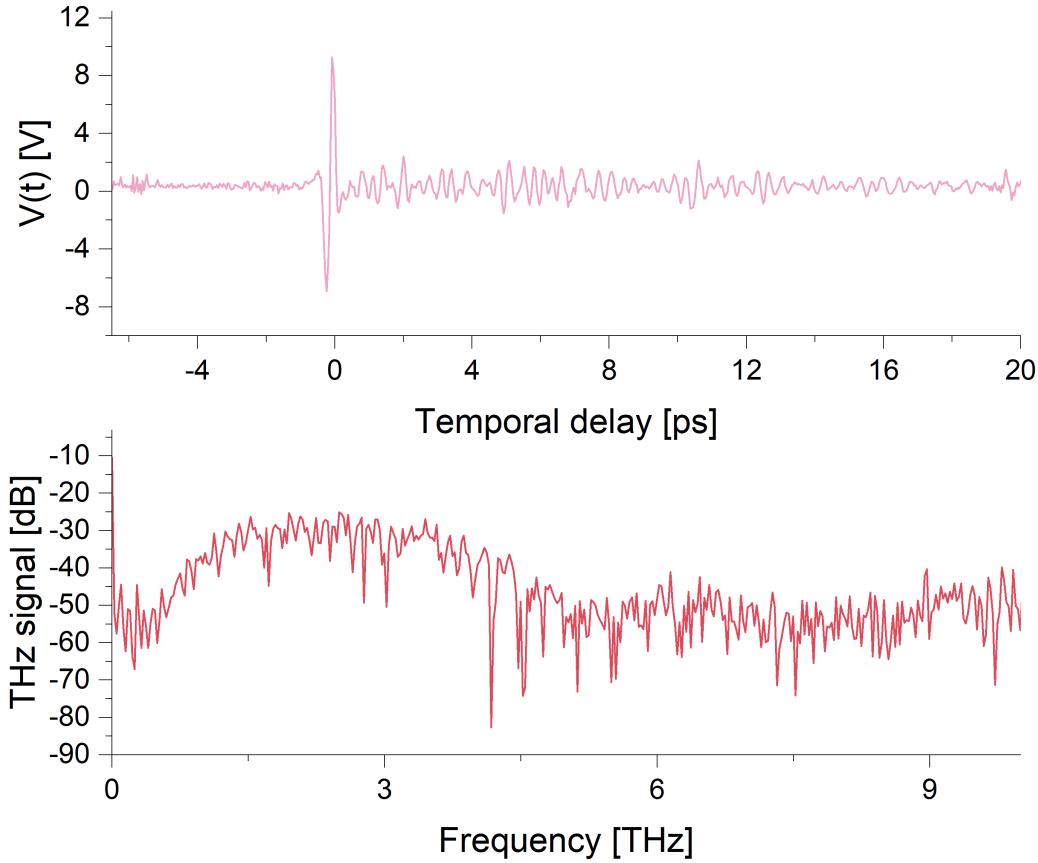

Figure 3.15: THz output signal in time and frequency domain. The considered signal is the tension coming from the LIA in time domain and its fast fourier transform in frequency domain.

The zero point in both images represents the point on the linear stage where the temporal and spatial delay between probe and THz beam is zero.

It is evident that the first measure is excessively impacted by noise and that the THz signal is not as good as in the second measure: this is especially clear by looking at the difference between the two signals in the frequency domain.

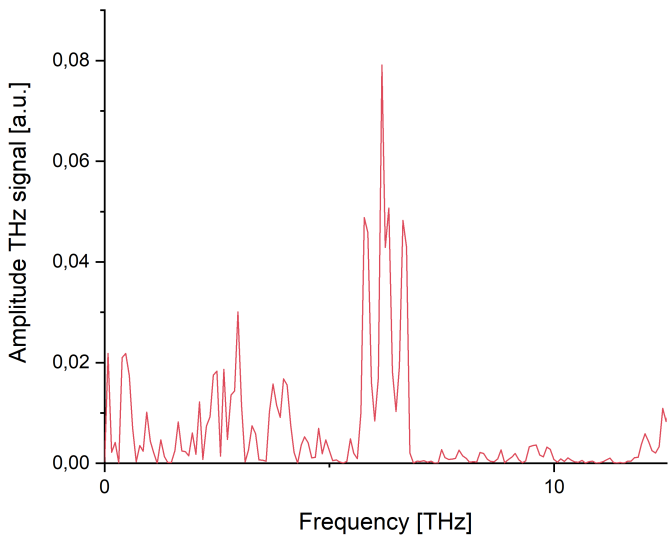

(a) THz signal in frequency domain of 3.14 plotted on a linear scale.

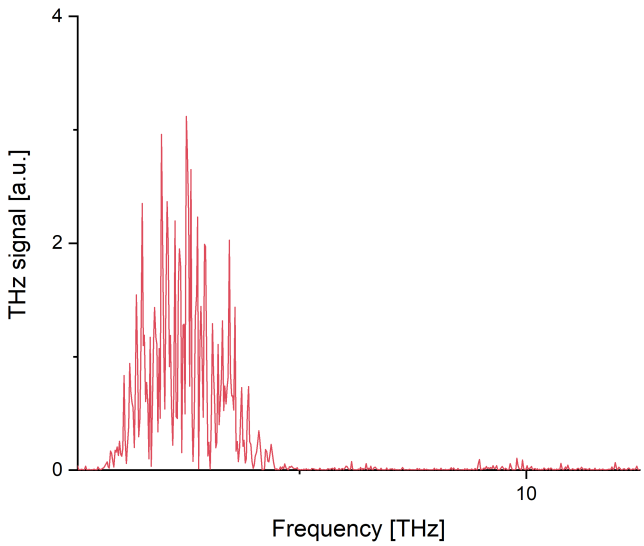

(b) THz signal in frequency domain of 3.15 plotted on a linear scale.

Figure 3.16: Comparison of signal obtained from two different measures.

The steps taken to improve the signal were: we adjusted the polarisation of the generating beam using a polariser; we again checked that the two crystals used were in the actual focus of the lens and parabolic mirrors; we improved the collimation of THz radiation by acting on the position and orientation of the first parabolic mirrors; we finally adjusted the superposition of the THz and probe beam by acting on the second parabolic mirror.

Still, even with all the adjustments, the thing that we could only partially improve was the noisiness of the signal, being limited by the maximum modulation frequency obtainable by a mechanical chopper, in our case $10kHz$. One possible solution to the problem could be choosing a different modulating device, able to reach much higher frequencies, effectively reducing the noise coming from the laser source and the PCF (see image 3.13b); for this reason it could be helpful to try and improve the measures by using an acusto-optic modulator (AOM) instead of the chopper.

4 | Conclusions and future developments

For this master thesis we designed and realised a system for THz radiation generation and detection exploiting non-linear optical effects, namely: optical rectification in a GaP crystal for generation and electro-optical sampling for detection. Starting from a fiber laser delivering ultra-short pulses, We exploited a photonic crystal fiber and a pair of chirped mirrors to broaden the spectrum of the laser radiation and to compensate for any increase in time duration caused by the elements of the setup. The main limit to this solution is power loss, mostly caused by the fiber, which in our system was about 20% of the total. THz radiation was then obtained by focusing the broadened radiation on a GaP crystal, making sure to minimise the size of the generating spot, and to impinge on the crystal with the right polarisation with respect to the crystal geometry. To detect the generated THz radiation via electro-optical sampling another GaP crystal was used. In this case the most challenging part was making sure to obtain a good superposition, temporally and spatially, between probe and THz radiation. Thanks to focusing, the two were made to be of similar dimension once impinging on the electro-optical crystal. In the end, despite of the noise, mostly induced by the laser and the PCF, we were able to obtain a good THz signal, both in time and frequency domain, centered at about $3THz$.

In the future, to improve the quality of the measures, one might try to modulate the signal at frequencies in the range of few MHz, so to limit the impact of noise on the output. Also the system can be used for spectroscopy applications, it is in fact possible to insert a sample in between the two parabolic mirrors used to focus THz radiation, as it is the only kind of radiation present in the area.

Bibliography

[1] B.-H. Chen. *Single-cycle mid-infrared pulse generation via nonlinear optics*. PhD thesis, Ludwig Maximilians Universität München, 2019.

[2] J. M. Dudley and J. R. Taylor. *Supercontinuum generation in optical fibers*. Cambridge University Press, 2010.

[3] L. S. P. Frank L. Pedrotti. *Introduction to optics*. Prentice-Hall International inc., 1993.

[4] D. G. G. Gallot. Electro-optic detection of terahertz radiation. *J. Opt. Soc. Am.*, 1999.

[5] M. J. E. Golay. Radiation detecting device. June 1951.

[6] C. A. S. Jens Neu. Tutorial: An introduction to terahertz time domain spectroscopy (thz-tds). *J. Appl. Phys. 21 December 2018*, 2018. doi: https://doi.org/10.1063/1.5047659.

[7] H. C. Joo-Hiuk Son, Seung Jae Oh. Potential clinical applications of terahertz radiation. *J. Appl. Phys.*, 125, 2019. doi: https://doi.org/10.1063/1.5080205.

[8] J.-L. C. Lionel Duvillaret, Frederic Garet. Influence of noise on the characterization of materials by terahertz time-domain spectroscopy. *J. Opt. Soc. Am.*, 2000. doi: https://doi.org/10.1364/JOSAB.17.000452.

[9] H. Liu, W. Bai, J. Feng, and W. Jie. The synthesis of large-diameter znte crystal for thz emitting and detection. *Journal of Crystal Growth*, 475, 2017.

[10] J. Manzolli. Design and characterization of a compact terahertz spectrometer based on the optical sampling by cavity tuning method. Master's thesis, Politecnico di Milano, Politecnico di Milano, 2021.

[11] A. Mazzanti. Terahertz generation by optical rectification in an enhancement cavity of femtosecond ti:sa laser. Master's thesis, Politecnico di Milano, The address of the publisher, 2016.

[12] *Onefive aeropulse FS20*. NKT Photonics, 6 2019.

[13] A. Y. Pawar, D. D. Sonawane, and K. B. E. D. V. Derle. Terahertz technology and its applications. *Drug Invention Today*, 5(2):157–163, 2013. ISSN 0975-7619. doi: https://doi.org/10.1016/j.dit.2013.03.009. URL `https://www.sciencedirect.com/science/article/pii/S0975761913000264`.

[14] C. Q., T. M., J. Zhiping, and Z. X.-C. Electro-optic transceivers for terahertz-wave applications. *Journal of the Optical Society of America B*, 18, 2001. doi: 10.1364/JOSAB.18.000823.

[15] A. E. L. R Vasantha Jayakantha Raja. *Fiber Optic Pulse Compression*. 2053-2563. IOP Publishing, 2022. ISBN 978-0-7503-2686-5. doi: 10.1088/978-0-7503-2686-5.

[16] I. Rech and G. Acconcia. *Signal recovery*. Pre-print, 2022.

[17] M. O. Rongqing Hui. Chapter 3 - characterization of optical devices. In R. Hui and M. O'sullivan, editors, *Fiber-Optic Measurement Techniques (Second Edition)*, pages 297–446. Academic Press, second edition edition, 2023. ISBN 978-0-323-90957-0. doi: https://doi.org/10.1016/B978-0-323-90957-0.00001-1. URL `https://www.sciencedirect.com/science/article/pii/B9780323909570000011`.

[18] X. Ropagnol, M. Matoba, J. Nkeck, F. Blanchard, E. Isgandarov, J. Yumoto, and T. Ozaki. Efficient terahertz generation and detection in cadmium telluride using ultrafast ytterbium laser. *Applied Physics Letters*, 117(18), 2020.

[19] A. Schneider, M. Neis, M. Stillhart, B. Ruiz, R. Khan, and P. Gunter. Generation of terahertz pulses through optical rectification in organic dast crystals: Theory and experiment. *Journal of the Optical Society of America B*, 23:1822, 04 2006. doi: 10.1364/JOSAB.23.001822.

[20] O. Svelto. *Principles of lasers*. Springler, 4 edition, 1998. doi: https://doi.org/10.1007/978-1-4757-6266-2.

[21] K. Tian, L. He, X. Yang, and H. Liang. Mid-infrared few-cycle pulse generation and amplification. In *Photonics*, volume 8, page 290. MDPI, 2021.

[22] S. S. e. a. Tomasino A., Parisi A. Wideband thz time domain spectroscopy based on optical rectification and electro-optic sampling. *Sci Rep 3*, 2013. doi: https://doi.org/10.1038/srep03116.

[23] A. M. Weiner. *Ultrafast optics*. 2053-2563. Wiley, 2008. ISBN 9780471415398. doi: 10.1002/9780470473467.

[24] D. J. Wilson, K. Schneider, S. Hönl, M. Anderson, Y. Baumgartner, L. Czornomaz, T. J. Kippenberg, and P. Seidler. Integrated gallium phosphide nonlinear photonics. *Nature Photonics*, 14(1), 2020.

[25] W. Withayachumnankul, B. M. Fischer, H. Lin, and D. Abbott. Uncertainty in terahertz time-domain spectroscopy measurement. *J. Opt. Soc. Am. B*, 25(6):1059–1072, Jun 2008. doi: 10.1364/JOSAB.25.001059. URL `https://opg.optica.org/josab/abstract.cfm?URI=josab-25-6-1059`.

[26] J. X. Xi-Chang Zhang. *Introduction to THz Wave Photonics*. Springer New York, NY, 1 edition, 2010. doi: https://doi.org/10.1007/978-1-4419-0978-7.

A | Appendix A: methods and instruments

A.1. Golay cell

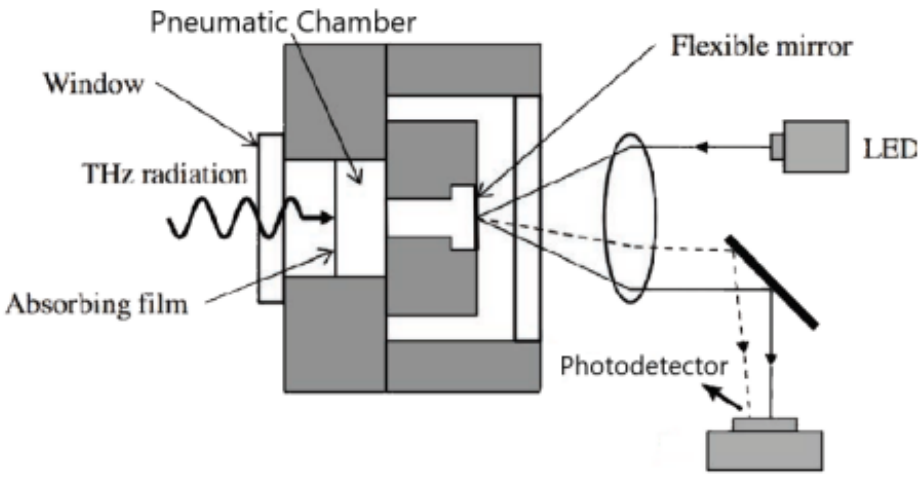

Figure A.1: Schematic of a Golay cell. [10]

A Golay cell is a opto-acoustic detector for infrared radiation composed of a pneumatic part and an optical part. In the first part there is a chamber filled with gas, which expands when radiation is absorbed as a result of the increase of its temperature; the expansion of the gas deforms a reflecting diaphragm. In the optical part there is a fixed light source which is reflected by the diaphragm into a photodiode. The change in the shape of the reflecting surface causes a change in the amount of light reaching the photodetector, generating the output signal.[5]

A.2. Lock-in amplifier

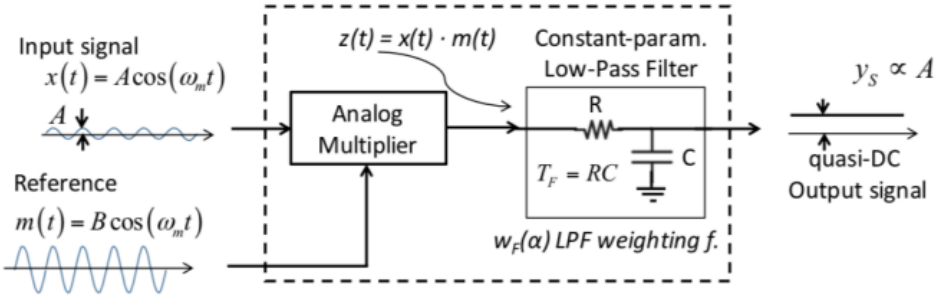

Figure A.2: LIA schematic. [16]

The working principle of a lock-in amplifier is simple: the input signal $x(t)$ is multiplied by a reference signal $m(t)$ with same frequency. The resulting signal $z(t)$ is then integrated over a small time period so to obtain a DC, or approximately so, output signal $y(t)$.

$$y(t) = \int_0^\infty x(\alpha)m(\alpha)w_F(\alpha)d\alpha \tag{A.1}$$

A.3. Auto-correlator

When dealing with femto-second pulses we can't rely on electronics to compute their duration. One way to circumvent this problem is by computing the pulses' auto-correlation.

In the auto-correlator, the beam is split and the two newly formed pulses propagate through two different paths, one of which contains a variable delay stage τ. The two pulses are then focused on a SHG crystal through a lens; once the crystal is tilted in the direction of the wave vector of one of the two pulses, their two second harmonics are generated. If the delay between the two pulses is close to zero, then they impinge on the crystal virtually at the same time and thus generate an ulterior second harmonic beam with wave vector equal to the sum of the other two (granted that we are in phase matching condition). This new beam passes through an iris so that all the unwanted spectral components are filtered, leaving only the wave vector direction needed, then a photo multiplier tube is used to reveal its intensity.

Let's call $E_1(t)$ and $E_2(t)$ the two electric fields associated to the beams impinging on the crystal, the second harmonic generated can be written as:

$$E_{SH}(t,\tau) = \gamma E_1(t,\tau)E_2(t,\tau) = \gamma E(t)E(t-\tau) \tag{A.2}$$

with γ general proportionality factor and E the original field. The detector will then measure the energy of the second harmonic pulse as a function of the delay τ:

$$U_{SH}(\tau) = \int_{-\infty}^{+\infty} |E_{SH}(t,\tau)|^2 dt \propto \int_{-\infty}^{+\infty} I(t)I(t-\tau)dt = C_I(\tau) \tag{A.3}$$

with I intensity of the laser beam entering the auto-correlator and $C_I(\tau)$ intensity auto-correlation.

$C_I(\tau)$ has its peak at $\tau = 0$ and is always an even function, this mean that we can get the time duration of the pulse intensity $\delta\tau_p$ by measuring the time duration of the auto-correlation $\delta\tau_{FWHM}$, as they are linked by the following:

$$\delta\tau_p = \frac{\delta\tau_{FWHM}}{a} \tag{A.4}$$

with a a-dimensional factor that depends on the shape of the pulse and is always bigger than 1. [10]

B | Appendix B

B.1. Matlab script for measures

The following is the Matlab script used to obtain the measures of THz signal as reported in 3.6.

```
close all

clc

% ACQUISITION PARAMETERS

tau_LIA = 0.5; % s ,time constant as set on LIA

NN = 500; % total steps taken by linear stage

MM = 1; % number of back to back acquisition wanted

first_step = -15000; % um

step_translation_stage = 60; % um

c = physconst('LightSpeed');

ii = 1;

kk = 1;

ll = 1;

fin_data = zeros(1,NN,MM);

f = zeros(1, NN);

avg_data = zeros(1,NN);

V = zeros(NN, 2);

A = zeros(NN, 2);

% SET THE TRANSLATION STAGE
```

```
obj1=instrfind('Type', 'gpib', 'Boardindex', 0, 'PrimaryAddress', 2, 'Tag', '');
% CREATE THE GPIB OBJECT OR USE THE ONE FOUND
if isempty(obj1)
obj1 = gpib('NI', 0, 2);
else fclose(obj1);
obj1 = obj1(1);
end
fopen(obj1);
% CHANNEL CONFIGURATION
s = daq.createSession('NI');
addAnalogInputChannel(s, 'Dev1', 'ai0', 'Voltage');
% SET ACQUISITION PROPERTIES
s.Rate = 2000; % Sampling frequency
s.DurationInSeconds = 0.1; % acquisition duration, s
% X-AXIS DEFINITION FOR GRAPHS
step_tau=2*step_translation_stage/c; % s
fin_pos=(NN-1)*step_translation_stage+first_step; % final position reached by linear stage
x_axis=[first_step : step_translation_stage: fin_pos];
% START OF ACQUISITION
disp('Starting Acquisition');
for b=1:1:MM % allows multiple back to back acquisition to average
fprintf(obj1, 'XGR -15000'); % um, moves to starting point
for a=1:1:NN
fprintf(obj1, 'XGR 60'); % um, moves the linear stage of 60um with respect to previous point
data1 = query(obj1, 'xg?'); % asks for position and saves value
```

```
pause(tau_LIA);
% DATA ACQUISITION
[data, data1] = startForeground(s); % acquires Voltage data and pairs it to position data
fin_data(1,ii,kk) = mean(data); % Voltage average
ii = ii + 1;
if kk==1
figure(2);
plot(x_axis, fin_data(1,:,kk)); % allows real time plotting
else %allows real time plotting in case of multiple acquisition keeping previous ones in graph
plot(x_axis, fin_data(1,:,1)); hold on
plot(x_axis, fin_data(1,:,kk));
hold off
end
end
avg_data = (avg_data + fin_data(1,:,kk));
kk = kk + 1;
ii = 1;
fprintf(obj1, 'XG 0'); % sends linear stage back to position zero
end
kk=1;
avg = avg_data/MM; % averages multiple acquisition
disp('Stop Acquisition');
s.stop();
% PLOTS TIME DOMAIN SIGNAL
f1=figure(1);
plot(x_axis, avg, 'm');
```

```
V = [transpose(x_axis) transpose(avg)];
writematrix (V, 'VvsTau_Thz_noise7.dat'); % Saves data on computer
xlabel('Posizione su slitta (um)');
ylabel('Tensione (V)');
N = length(avg); % Number of samples for fft
X = fft(avg)/N; % Normalised fft
f = [0:1:(N-1)]*(1/(N*step_tau*1e6)); % Frequency vector
% AMPLITUDE, PHASE, POWER OF FFT
amplitude = abs(X);
phase = angle(X);
power_spectrum = abs(X).^2;
% PLOTS FFT
f2=figure;
subplot(3,1,1);
amplitude_dB = 10*log(amplitude);
plot(f, amplitude_dB);
A = [transpose(f) transpose(amplitude_dB)];
writematrix(A, 'AvsF_THz_noise7.dat'); % Saves data on computer
xlabel('Frequenza [THz]');
ylabel('Ampiezza [dB]');
subplot(3,1,2);
plot(f, phase);
xlabel('Frequenza [THz]');
ylabel('Fase [rad]');
subplot(3,1,3);
power_spectrum_dB = 10*log(power_spectrum);
```

```
plot(f, power_spectrum_dB);
xlabel('Frequenza [THz]');
ylabel('Modulo quadro [dB]');
pause(1)
fprintf(obj1, 'XG 0');
pause(1)
fprintf(obj1, 'XM');
fclose(obj1); % Closes connection to translation stage
```

List of Figures

1.1 Comparison between DFG and iDFG; for iDFG the pump ω_1 and the seed ω_2 come from the same pulse, ω_3, the idler, corresponds to their difference $\Delta\omega$. The frequencies in between do not participate in the process.[1] 8

1.2 Example of diffraction transfer function dependent on frequency, represented with a continuous red line. The frequencies below $2.2THz$, being valid $k_{THz}w_{THz} < 1$ behave as predicted by Bethe's scattering, whereas the frequencies above, when $k_{THz}w_{THz} > 1$, behave as predicted by Rayleigh's scattering.[22] 10

1.3 Example of how the frequency range affected by Bethe scattering grows with the decrease of the waist beam size. While with smaller beams, a broader frequency range tends to diffract following Bethe's theory, still they produce a stronger THz field compared to larger beams.[22] 11

1.4 Transfer function of the focusing stage, depending on the frequency of the generated radiation and on beam size.[22] 12

1.5 Geometry of the (110) zinc-blende crystal. [14] 14

1.6 Real (left) and imaginary (right) refractive index of GaP. [11] 15

1.7 Coherence length depending frequency with 800 nm excitation. [11] 16

1.8 THz generation in (110) CdTe with respect to wavelength of pump. [11] . . 17

1.9 Spectra of THz radiation generated in DAST crystal. The solid line corresponds to a pump with $\lambda = 740nm$, the dashed one to a pump with $\lambda = 710nm$.[11] 18

1.10 General Scheme of an ellipsometer.[4] 21

1.11 Comparison between circular (dashed line) and elliptical polarisation obtained after the $\lambda/4$ plane.[4] 22

1.12 Geometry of the (110) crystal for EO sampling.[14] 25

1.13 Example of a two layer system used for THz spectroscopy. The system can be considered to be in air ($n_0 = n_3 = 1$) for simplicity. n_1, d_1 refer to the substrate while n_2, d_2 refer to the sample under observation.[6] 27

1.14 Example of sample tilted with respect to the optimal position, orthogonal to the impinging radiation.[25] 32

2.1 Gaussian distribution of spectral amplitudes of different modes.[20] 36
2.2 Modulator transmission. The resulting pulses are centered around the peaks of the modulator transfer function.[20] 37
2.3 Fast saturable absorber mode-locking. Mode-locking condition is met when absorption drops below the gain line, considered constant.[20] 38
2.4 General structure of fiber used for cladding pumping.[20] 39
2.5 General schematic of a silica photonic crystal fiber. In the image the key structural parameters are highlighted. [15] 40
2.6 Group index, refractive index and group velocity dispersion D for bulk silica, plotted with respect to the wavelength of radiation propagating through it.[2] 42
2.7 General structure of a chirped mirror with negative dispersion D.[23] . . . 45
2.8 General scheme depicting the working principle behind parallel grating pair.[23] 46

3.1 Broadened spectrum of laser radiation with rr=25MHz. 49
3.2 Broadened spectrum of laser radiation with rr=50MHz. 49
3.3 Auto-correlation of shortened laser pulses. The FWHM is $90fs$, indicating a pulse duration of $60fs$. 50
3.4 51
3.5 Complete experimental setup. CM stands for Chirped Mirrors, HR for High reflectivity, PCF for photonic crystal fiber, PM for parabolic mirror, T is the transmission coefficient of the output coupler. 52
3.6 Beam profile without lens. 53
3.7 Beam profile with lens. 53
3.8 Setup to measure THz using the Golay cell. 54
3.9 Golay output signal versus power of laser beam. 55
3.10 Second of the experimental setup, used for EO sampling. 56
3.11 Shorter caption 57
3.12 Shorter caption 58
3.13 Laser RIN before and after PCF. 60
3.14 THz output signal in time and frequency domain. The considered signal is the tension coming from the LIA in time domain and its fast fourier transform in frequency domain. 62

3.15 THz output signal in time and frequency domain. The considered signal is the tension coming from the LIA in time domain and its fast fourier transform in frequency domain. 63
3.16 Shorter caption 64

A.1 Schematic of a Golay cell. [10] 73
A.2 LIA schematic. [16] 74

List of Symbols

Variable	Description	SI unit
c	solid displacement	ms^{-1}
ϵ_0	vacuum permittivity	Fm^{-1}
μ_0	vacuum permeability	$kgms^{-2}A^{-2}$
χ	magnetic susceptibility	adim.
σ	charge density	Cm^{-3}

Acknowledgements

I would like to thank my advisor, Prof. Alessio Gambetta, and my co-advisor, Prof. Nicola Coluccelli, for their much appreciated help. I would also like to thank Dott. Giovanni Cichelli for its support during laboratory activity, and for showing me how to work in one. Finally I thank my family and friends for their constant, loving support.